Oil & Natural Gas Technology

DOE Award No.: DE-FE0024297

Quarterly Research Performance

Progress Report (Period Ending 6/30/2019)

Marcellus Shale Energy and Environment Laboratory (MSEEL)

Project Period (October 1, 2014 – September 30, 2019)

Submitted by:
Samuel Taylor

Signature

West Virginia University Research Corporation
DUN's Number: 191510239
886 Chestnut Ridge Road,
PO Box 6845, Morgantown WV, 26505
Tim.Carr@mail.wvu.edu
304-293-9660

Prepared for:
United States Department of Energy
National Energy Technology Laboratory

6/30/2019

U.S. DEPARTMENT OF ENERGY | NATIONAL ENERGY TECHNOLOGY LABORATORY

Office of Fossil Energy

Executive Summary
Quarterly Progress Report

April 1 – June 30, 2019

The objective of the Marcellus Shale Energy and Environment Laboratory (MSEEL) is to provide a long-term field site to develop and validate new knowledge and technology to improve recovery efficiency and minimize environmental implications of unconventional resource development.

Plans developed for MSEEL Phase 3 are being executed at the Boggess Pad just west of Morgantown, WV. The Boggess pad consisting of six wells was selected. This quarter work focused on the spudding and drilling of MSEEL Phase 3 wells at the Boggess Pad. As of this report, drilling is complete, and stimulation/completion is planned to begin later this summer, using input from the MSEEL team. Drilling expansion and research on machine learning for improved production efficiency were approved by DOE for inclusion into the project, through completion in early 2021. Project overviews were presented to the Marcellus Shale Coalition annual meeting in June 2019, URTeC Regional in Pittsburgh and preparations are underway for several papers at URTeC in July 2019.

We have worked to process the data from the downhole microseismic sensors and the fiber-optic data to better understand geomechanical properties and slow slip events during hydraulic fracture stimulation. Prepared manuscript for URTeC in July 2019.

Project Performance

This report summarizes the activities of Cooperative Agreement DE-FE0024297 (Marcellus Shale Energy and Environment Laboratory – MSEEL) with the West Virginia University Research Corporation (WVURC) during the third quarter of FY2019 (April 1 through June 30, 2019).

This report outlines the approach taken, including specific actions by subtopic. If there was no identified activity during the reporting period, the appropriate section is included but without additional information.

A summary of major lessons learned to this point of the project are provided as bullet points and will be added to as research is completed. New lessons listed below are:

Phase 3 Plans

A phase 3 of MSEEL is moving forward with drilling and completion. Drilling of the pilot hole and laterals began 8 April and completed on 30 June. Completion is scheduled to begin at the end of July. Six 10,000+ foot horizontal Marcellus Shale wells off a single pad (Boggess) have been drilled very near the initial MIP pad (Figure 1.1), with stimulation and completion planned for late summer 2019. The pad will have at one permanent fiber optic (FO) cable installed that will provide digital acoustic sensing (DAS) during stimulation and distributed temperature sensing (DTS) during stimulation and long-term production monitoring along the lateral (Boggess 5H). Two deployable FO systems are also proposed (Boggess 1H and 17H). This will permit evaluation of stimulation effectiveness in near real-time and the 100's of terabytes of data to evaluate and model the reservoir across each individual stage, and at individual clusters within stages for 3 wells. The deployable fiber in parallel wells (skipping one adjacent) will allow excellent microseismic imaging, recognition and evaluation of long-period long-duration events in the test well. We will also be able to monitor adjacent wells to the test well during stimulation. We have developed techniques to use the permanent DAS and DTS monitoring in the 5H to determine production rates and changes at the stage level through the life of the well.

The cored and logged vertical pilot well is being evaluated to develop a high-resolution geomechanical model (stratigraphy) to type each 6 inches of the Marcellus. A total of 139.2 feet of four-inch core and 50 large diameter sidewall cores were recovered from the vertical 17H pilot. All core material being analyzed at NETL, WVU and commercially. All six laterals were successfully drilled by the end of June, and excellent logging while drilling (LWD) data was recovered. Logging while drilling (LWD) logs in each of the six laterals provide similar geomechanical logs and image logs to geomechanically type each foot of the laterals as the horizontal laterals move stratigraphically up and down through the Marcellus. This approach permits direct coupling and evaluation of cost-effective LWD technologies to the relatively high-cost permanent FO data and the basis for engineering stages in all wells. Data is being analyzed by WVU and by commercial consultants to design an improved completion.

The plan remains to complete at least two of the laterals with the standard industrial geometrical completion practice (identical 200 feet stages with identical number of clusters in each stage). These will be the control wells. We will use the LWD and permanent FO in the one well (extremely large big data) along with active proppant and the LWD and microseismic only (relatively "thin" data) in the other wells to engineer stage and cluster spacing. Coupled with production data from all the wells including the control wells, this provides the basis to evaluate

the reservoir through modeling and direct monitoring to develop a first ever, publicly available, multi-well unconventional fractured reservoir simulation.

MSEEL 2 will compare across the six wells and with the MIP pad (MSEEL 1) and use these data to form the basis for robust big data modeling. MSEEL 1 generated almost 10 terabytes of data and created approaches and capabilities to handle and process big data sets (i.e., volume, variety, velocity and veracity) from a single well to address the spacing between laterals and stage length, the importance of modeling at multiple scales from nanopores in kerogen to healed fractures spaced along the lateral, and the approaches to engineering stage and cluster design and stimulation processes. The multiple wells at MSEEL 2 and the new generation high resolution fiber and LWD tools will provide 100's of terabytes of data in a series of similar wells under controlled conditions to test and enhance the understanding of shale reservoirs, MSEEL 2 will test new technologies and approaches to provide robust models that can be modified in near real-time using "thick" relatively high-cost data sets limited to science wells, or when calibrated more cost-effective "thin" data sets that could be used in broader field development and basin evaluation.

Numerous tours were undertaken for a variety of people. Tours and dates include:

- 4-17-19 Federal Government
- 4-18-19 WVU Law
- 4-19-19 Argentinian Engineering Program
- 4-25-19 Geology Students WVU
- 5-1-19 NNE Office Personnel
- 5-3-19 WVU Administration and Faculty
- 5-8-19 NETL FAC
- 5-9-19 NETL FAC
- 5-15-19 WVU Land Management
- 5-16-19 WV Women Work
- 6-18-19 Land Management WVU

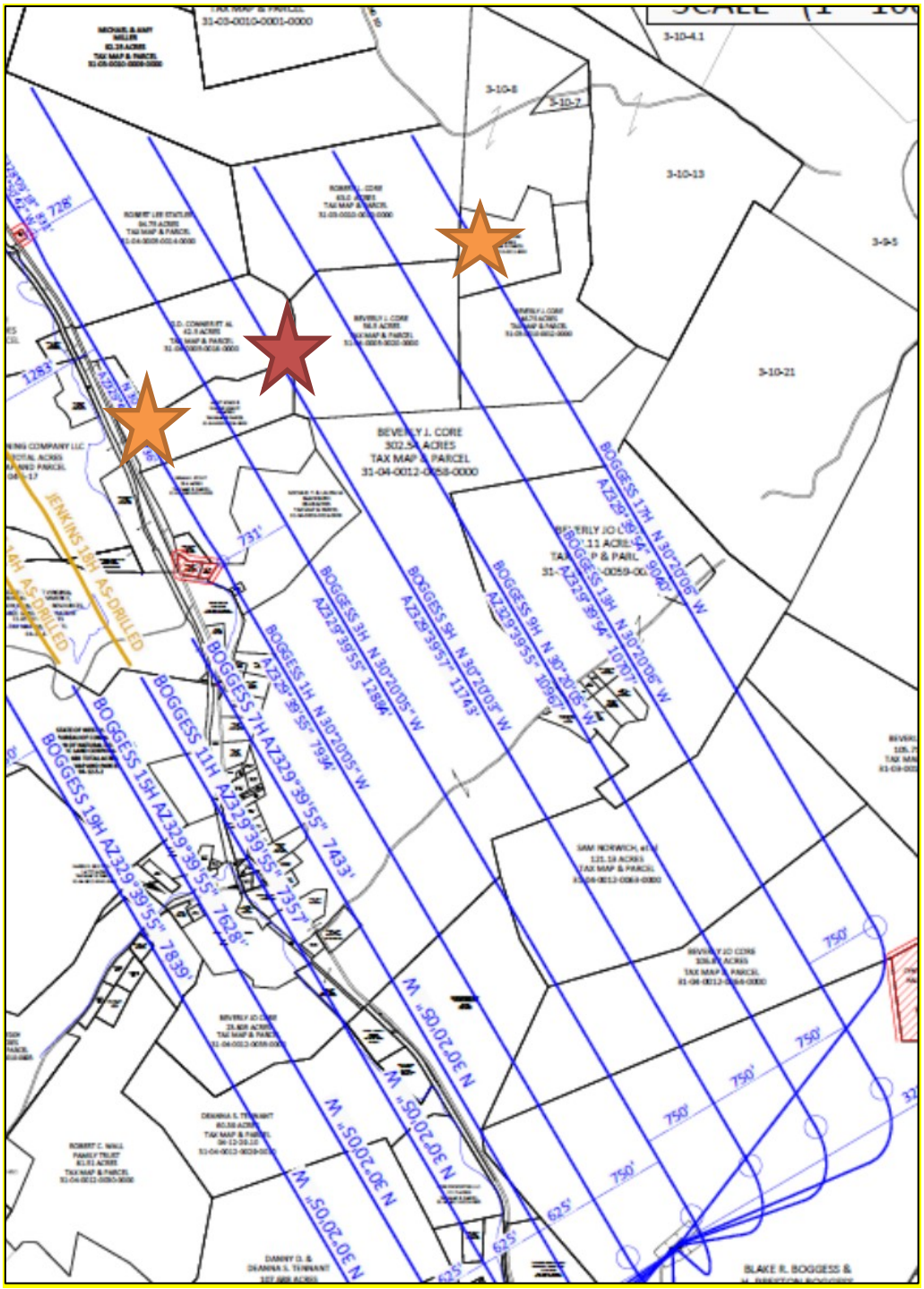

Figure 1.1: Boggess Pad with new generation permanent fiber in the central well (Boggess 5H, red star)) and deployable fiber in adjoining wells skipping one (orange stars). We will be able to monitor in near-real time fracture stimulation in the central 3 wells (3H, 5H and 9H). A vertical pilot will be drilled, cored and logged.

Project Management Update

Approach

The project management team will work to generate timely and accurate reporting, and to maintain project operations, including contracting, reporting, meeting organization, and general oversight.

Results and Discussion

The project team is tracking eight (8) milestones in this budget period.

	Task	Milestone	Status	Due Date
1.	3.2.1	Methane Audit 10 Completed	Complete	5/31/2019
2.	3.2.1	Sample collection and analysis of horizontal drill cuttings and drilling mud	Complete 139.2' of core and core plugs were collected from the vertical 17H pilot well. Drilling fluids collected.	6/30/2019
3.	3.2.1	Sample collection and analysis of makeup water and frac fluids	Samples will be collected from Boggess Wells	9/30/2019
4.	3.2.1	Eddy Covariance Methane Detection Deployed at Wellsite (MIP)	New methane detection approach will be field tested at the MIP site on producing wells.	9/30/2019
5.	3.1.3	Boggess wells turned in.	Boggess wells are scheduled to be completed and turned in Oct 2019	10/31/2019
6.	3.1.2	Characterization of organic matter - Total Organic Carbon and Pyrolosis Experiments Complete	Characterization of samples from Boggess wells.	12/31/2019
7.	3.1.2	Isotopic characterization of produced water and gases - sampling and analysis complete	Characterization of produced water and samples from Boggess Wells	12/31/2019
8.	3.1.3	Provide final DAS/DTS data from completion activities to researchers (Boggess)	Final DAS/DTS data from well completion will be available to researchers.	12/31/2019

	3.2.1	Sample collection and analysis of flowback/produced water	Characterization of produced water and samples from Boggess Wells	12/31/2019
	3.2.1	Energy Audit System Deployed with Patterson Rig (Boggess)	CAFEE team members will deply energy audit equipment with the Patterson drilling rig. Activity is focused on cold weather months. Location is likely not Boggess specifically, but will follow field activities.	12/31/2019
	3.4.1	Statistical Analysis of production stages complete	Initial data analysis for Machine Learning Tasks.	12/31/2019

Topic 1 – Geologic Engineering

Approach

In addition to advances in improving our understanding of chemical evolution of produced water, methane emissions, microbiology and rock-fluid geochemistry, we continue to work to better understand the microseismic monitoring by downhole geophones, surface seismic, fiber-optic distributed acoustic sensing (DAS), and distributed temperature sensing (DTS) observations made during the hydraulic fracture stimulation of the MIP-3H well. DAS and DTS data measure the fiber strain and temperature, respectively, along a fiber-optic cable cemented behind the casing of the well. The presence of long-period long-duration (LPLD) events as picked up on surface sensor employed by NETL (Kumar et al. 2017) were evaluated in the borehole geophones, DAS data, and surface seismic data of one of the MIP-3H stimulated stages. LPLD events are generally overlooked during the conventional processing of microseismic data, but they represent significant nonbrittle deformation produced during hydraulic fracture stimulation. In a single stage that was examined, 160 preexisting fractures and two faults of suboptimal orientation are noted in the image logs. We identified two low-frequency (<10 Hz) events of large temporal duration (tens of seconds) by comparing the surface seismic data, borehole geophone data, and DAS amplitude spectra of one of the MIP-3H stages. Spectrograms of DAS traces in time and depth reveal that the first low-frequency event might be an injection noise that has footprints on all DAS channels above the stimulated stage. However, the surface seismic array indicates an LPLD event concurrent with the first low-frequency event on DAS. The second LPLD event on DAS data and surface seismic data is related to a local deformation and does not have footprints on all DAS channels. The interpreted events have duration less than 100 s with frequencies concentrated below 10 Hz and accompanied by microseismic events. We will test these results in the advanced fiber deployed at the Boggess pad.

Kumar, A., E. V. Zorn, R. Hammack, and W. Harbert, 2017a, Seismic monitoring of hydraulic fracturing activity at the Marcellus shale energy and environment laboratory (MSEEL) Site, West Virginia: Presented at the Unconventional Resources Technology Conference, Paper 2670481.

Results and Discussion

Presented an overview of the MSEEL project at the URTeC Regional Meeting, Pittsburgh, PA (April 15th).We presented the results of the DAS analysis at the American Rock Mechanics Association (ARMA) Annual Meeting in New York City as an invited lecture at the Workshop entitled *Hydraulic Fracturing Efficient Energy: Observations, Monitoring and Diagnostics* (June 27th).

Products

Carr, Timothy R. MSEEL Seismic Attribute Application of Distributed Acoustic Sensing Data, presentation at 53rd US Rock Mechanics / Geomechanics Symposium, 2019 American Rock Mechanics Association (ARMA) Annual Meeting, New York City, NY.

Carr, Timothy R., Payam Kavousi Ghahfarokhi, BJ Carney, Jay Hewitt, and Robert Vagnetti, 2019, Marcellus Shale Energy and Environmental Laboratory (MSEEL) Results and Plans: Improved Subsurface Reservoir Characterization and Engineered Completions, URTeC 415, Paper prepared for presentation at the Unconventional Resources Technology Conference (URTeC) held in Denver, Colorado, USA, 22-24 July 2019, 10 pages, DOI 10.15530/urtec-2019-415.

Evans, Kaitlin, Randy Toth, Tobi Ore, Jarrett Smith, Natalia Bannikova Timothy Carr, and Payam Kavousi Ghahfarokhi, 2019, Fracture analysis before and after Hydraulic Fracturing in the Marcellus Shale using the Mohr-Coulomb failure criteria, URTeC 650,
Paper prepared for presentation at the Unconventional Resources Technology Conference (URTeC) held in Denver, Colorado, USA, 22-24 July 2019, 11 pages, DOI 10.15530/urtec-2019-650.

Plan for Next Quarter

Present two MSEEL papers at the 2019 Unconventional Resources Technology Conference URTeC in Denver, Colorado (July 22-24). Papers as published by SPE/AAPG/SEG are attached as Appendix A. One paper led by WVU graduate students at WVU was selected for a prestigious 50 minute presentation in the Exhibition Hall.

Develop software to analysis the LWD data in order to engineer stages and clusters that optimize completion and production in four wells and maintain two wells with standard geometric completions as control wells.

Topic 2 – Geophysical & Geomechanical

Approach

Geophysical and Geomechanical

During this quarterly period, the influence of a discrete fracture network on the growth of hydraulic fractures was investigated through the use of numerical modeling. The numerical model updated in a previous quarter was used to compute hydraulic fracture dimensions for stage 26 through stage 30 of well MIP-5H.

During this quarterly period, the influence of a discrete fracture network on the growth of hydraulic fractures was investigated through the use of numerical modeling. All numerical modeling results were synthesized along with microseismic data results.

Microseismic data was available for stages 7 through 28 at well MIP-3H and stages 2 and 5 through 30 at well MIP-5H. Microseismic, well, and hydraulic fracture geometry data were visualized in three dimensions. Figure 1 shows a side-view of well MIP-3H with all numerically modeled hydraulic fractures with available microseismic data. Figure 2 shows a side-view of well MIP-5H with all numerically modeled hydraulic fractures with available microseismic data. Figure 3 shows a top view of well MIP-3H with all numerically modeled hydraulic fractures with available microseismic data. Figure 4 shows a top view of well MIP-5H with all numerically modeled hydraulic fractures with available microseismic data. Figure 5 shows a top view of both wells MIP-3H and MIP-5H with all numerically modeled hydraulic fractures with available microseismic data.

The match between numerical model calculated fracture heights and lengths and microseismic estimated height and length data is not currently considered to be excellent. The current modeling study will be continued to evaluate the influence of geomechanical properties on fracture geometries in comparison to microseismic estimates. A statistical methodology is being explored to better reconcile numerical model calculated fracture heights and lengths, and microseismic height and length estimates.

Results & Discussion

During this quarterly period, the influence of several geomechanical/fluid flow properties on the vertical growth of hydraulic fractures was investigated through a sensitivity analysis. The calculated hydraulic fracture heights do not match very well with the microseismic cloud height estimates. Therefore, the influence of several key geomechanical and fluid flow properties was evaluated in the Marcellus Shale and the surrounding geologic layers to attempt to reconcile calculated hydraulic fracture heights with estimated microseismic cloud heights.

The following geomechanical and fluid flow properties were modified in an arbitrarily selected stage based on the initial values taken from field measurements or literature: horizontal stress gradient, Young's modulus, Poisson's ratio, and fluid leak off coefficient. Each of these geomechanical and fluid flow properties were modified by increasing their respective base value by 10% or decreasing their respective base value by 10%.

The following geologic layers were chosen to make modifications to their base geomechanical/fluid flow properties (listed from shallowest layer to deepest layer): Tully Limestone, Hamilton Shale, Upper Marcellus Shale, Cherry Valley Limestone, Lower Marcellus Shale, and Onondaga Limestone. These layers were chosen as they are those which are most

frequently identified to interact with induced hydraulic fractures. The Tully Limestone and the Onondaga Limestone are frequently noted as barriers to upwards and downwards hydraulic fracture growth, respectively.

A total of 48 cases were developed to evaluate the influence of each of the geomechanical and fluid flow properties in each of the geologic layers previously mentioned on hydraulic fracture height growth independently. Each of these 48 cases were numerically modeled and the hydraulic fracture height data was calculated. The percent difference between the original calculated hydraulic fracture heights and the modified geomechanical/fluid flow property calculated hydraulic fracture heights was then determined.

Table 2.1 shows the 48 cases with the respective geomechanical/fluid flow property, the property modification (plus or minus 10% modification from the base value), the geologic layer which the property was modified in, and the percent change in the hydraulic fracture height from the base hydraulic fracture stage property values. Table 1 is sorted by the geologic layer, from shallowest to deepest. Table 2 shows the same information, but sorted by the percent change in the hydraulic fracture height. Positive percentages indicate that the fracture height in the modified property case was higher than that of the base case.

As can be seen from Table 2.1 and Table 2.2, the height percent changes range from +21.1% to -8.7%. Based on these percent differences, the horizontal stress gradient can be seen to have the greatest impact on the vertical hydraulic fracture growth. Increasing or decreasing the horizontal stress gradient in the Tully Limestone layer (of the upper bounding layer of hydraulic fractures) appears to have the greatest impact on vertical hydraulic fracture growth in general. A 10% decrease in the horizontal stress gradient in the Tully Limestone layer results in a 21.1% increase in hydraulic fracture height growth. While a 10% increase in the horizontal stress gradient in the Tully Limestone layer results in a 7.4% decrease in hydraulic fracture height growth.

After performing the sensitivity analysis by modifying the geomechanical/fluid flow properties in the aforementioned geologic layers, it was concluded that the change in the hydraulic fracture height was not significant enough to match microseismic cloud height estimates. Based on this conclusion, it has been determined that a statistical methodology is necessary to further analyze and compare the calculated hydraulic fracture dimensions with those of the microseismic cloud estimates.

Table 2.1: Geomechanical/Fluid Flow Property Sensitivity Analysis Study Results – Sorted by Geologic Layer

Case	Geomechanical/Fluid Flow Property	Property Modification	Geologic Layer	Change in Fracture Height From Base Case
1	Horizontal Stress Gradient	Increase 10% from base	Tully Limestone	-7.4%
2	Horizontal Stress Gradient	Decrease 10% from base	Tully Limestone	21.1%
3	Young's Modulus	Increase 10% from base	Tully Limestone	0.6%
4	Young's Modulus	Decrease 10% from base	Tully Limestone	-0.7%
5	Poisson's Ratio	Increase 10% from base	Tully Limestone	0.1%
6	Poisson's Ratio	Decrease 10% from base	Tully Limestone	-0.1%
7	Leakoff Coefficient	Increase 10% from base	Tully Limestone	0.0%
8	Leakoff Coefficient	Decrease 10% from base	Tully Limestone	0.0%
9	Horizontal Stress Gradient	Increase 10% from base	Hamilton Shale	-8.7%
10	Horizontal Stress Gradient	Decrease 10% from base	Hamilton Shale	7.1%
11	Young's Modulus	Increase 10% from base	Hamilton Shale	2.1%
12	Young's Modulus	Decrease 10% from base	Hamilton Shale	-2.3%
13	Poisson's Ratio	Increase 10% from base	Hamilton Shale	0.2%
14	Poisson's Ratio	Decrease 10% from base	Hamilton Shale	-0.2%
15	Leakoff Coefficient	Increase 10% from base	Hamilton Shale	-0.3%
16	Leakoff Coefficient	Decrease 10% from base	Hamilton Shale	0.3%
17	Horizontal Stress Gradient	Increase 10% from base	Upper Marcellus	13.9%
18	Horizontal Stress Gradient	Decrease 10% from base	Upper Marcellus	-5.8%
19	Young's Modulus	Increase 10% from base	Upper Marcellus	0.5%
20	Young's Modulus	Decrease 10% from base	Upper Marcellus	-1.3%
21	Poisson's Ratio	Increase 10% from base	Upper Marcellus	-0.2%
22	Poisson's Ratio	Decrease 10% from base	Upper Marcellus	-0.2%
23	Leakoff Coefficient	Increase 10% from base	Upper Marcellus	-0.9%
24	Leakoff Coefficient	Decrease 10% from base	Upper Marcellus	0.1%
25	Horizontal Stress Gradient	Increase 10% from base	Cherry Valley	9.0%
26	Horizontal Stress Gradient	Decrease 10% from base	Cherry Valley	-6.3%
27	Young's Modulus	Increase 10% from base	Cherry Valley	-0.6%
28	Young's Modulus	Decrease 10% from base	Cherry Valley	-0.5%
29	Poisson's Ratio	Increase 10% from base	Cherry Valley	-0.4%
30	Poisson's Ratio	Decrease 10% from base	Cherry Valley	-0.3%
31	Leakoff Coefficient	Increase 10% from base	Cherry Valley	-0.1%
32	Leakoff Coefficient	Decrease 10% from base	Cherry Valley	-0.4%
33	Horizontal Stress Gradient	Increase 10% from base	Lower Marcellus	4.4%
34	Horizontal Stress Gradient	Decrease 10% from base	Lower Marcellus	-4.8%
35	Young's Modulus	Increase 10% from base	Lower Marcellus	-0.4%
36	Young's Modulus	Decrease 10% from base	Lower Marcellus	-0.5%
37	Poisson's Ratio	Increase 10% from base	Lower Marcellus	-0.2%
38	Poisson's Ratio	Decrease 10% from base	Lower Marcellus	-0.2%
39	Leakoff Coefficient	Increase 10% from base	Lower Marcellus	-0.1%
40	Leakoff Coefficient	Decrease 10% from base	Lower Marcellus	-0.3%
41	Horizontal Stress Gradient	Increase 10% from base	Onondaga Limestone	-2.1%
42	Horizontal Stress Gradient	Decrease 10% from base	Onondaga Limestone	0.2%
43	Young's Modulus	Increase 10% from base	Onondaga Limestone	0.0%
44	Young's Modulus	Decrease 10% from base	Onondaga Limestone	-0.6%
45	Poisson's Ratio	Increase 10% from base	Onondaga Limestone	-0.4%
46	Poisson's Ratio	Decrease 10% from base	Onondaga Limestone	-0.5%
47	Leakoff Coefficient	Increase 10% from base	Onondaga Limestone	-0.9%
48	Leakoff Coefficient	Decrease 10% from base	Onondaga Limestone	-0.2%

Table 2.2: Geomechanical/Fluid Flow Property Sensitivity Analysis Study Results – Sorted by Percent Change in Fracture Height from Base Case

Case	Geomechanical/Fluid Flow Property	Property Modification	Geologic Layer	Change in Fracture Height From Base Case
2	Horizontal Stress Gradient	Decrease 10% from base	Tully Limestone	21.1%
17	Horizontal Stress Gradient	Increase 10% from base	Upper Marcellus	13.9%
25	Horizontal Stress Gradient	Increase 10% from base	Cherry Valley	9.0%
10	Horizontal Stress Gradient	Decrease 10% from base	Hamilton Shale	7.1%
33	Horizontal Stress Gradient	Increase 10% from base	Lower Marcellus	4.4%
11	Young's Modulus	Increase 10% from base	Hamilton Shale	2.1%
3	Young's Modulus	Increase 10% from base	Tully Limestone	0.6%
19	Young's Modulus	Increase 10% from base	Upper Marcellus	0.5%
16	Leakoff Coefficient	Decrease 10% from base	Hamilton Shale	0.3%
13	Poisson's Ratio	Increase 10% from base	Hamilton Shale	0.2%
42	Horizontal Stress Gradient	Decrease 10% from base	Onondaga Limestone	0.2%
5	Poisson's Ratio	Increase 10% from base	Tully Limestone	0.1%
24	Leakoff Coefficient	Decrease 10% from base	Upper Marcellus	0.1%
8	Leakoff Coefficient	Decrease 10% from base	Tully Limestone	0.0%
43	Young's Modulus	Increase 10% from base	Onondaga Limestone	0.0%
7	Leakoff Coefficient	Increase 10% from base	Tully Limestone	0.0%
39	Leakoff Coefficient	Increase 10% from base	Lower Marcellus	-0.1%
6	Poisson's Ratio	Decrease 10% from base	Tully Limestone	-0.1%
31	Leakoff Coefficient	Increase 10% from base	Cherry Valley	-0.1%
48	Leakoff Coefficient	Decrease 10% from base	Onondaga Limestone	-0.2%
14	Poisson's Ratio	Decrease 10% from base	Hamilton Shale	-0.2%
22	Poisson's Ratio	Decrease 10% from base	Upper Marcellus	-0.2%
38	Poisson's Ratio	Decrease 10% from base	Lower Marcellus	-0.2%
21	Poisson's Ratio	Increase 10% from base	Upper Marcellus	-0.2%
37	Poisson's Ratio	Increase 10% from base	Lower Marcellus	-0.2%
40	Leakoff Coefficient	Decrease 10% from base	Lower Marcellus	-0.3%
15	Leakoff Coefficient	Increase 10% from base	Hamilton Shale	-0.3%
30	Poisson's Ratio	Decrease 10% from base	Cherry Valley	-0.3%
45	Poisson's Ratio	Increase 10% from base	Onondaga Limestone	-0.4%
29	Poisson's Ratio	Increase 10% from base	Cherry Valley	-0.4%
32	Leakoff Coefficient	Decrease 10% from base	Cherry Valley	-0.4%
35	Young's Modulus	Increase 10% from base	Lower Marcellus	-0.4%
28	Young's Modulus	Decrease 10% from base	Cherry Valley	-0.5%
36	Young's Modulus	Decrease 10% from base	Lower Marcellus	-0.5%
46	Poisson's Ratio	Decrease 10% from base	Onondaga Limestone	-0.5%
27	Young's Modulus	Increase 10% from base	Cherry Valley	-0.6%
44	Young's Modulus	Decrease 10% from base	Onondaga Limestone	-0.6%
4	Young's Modulus	Decrease 10% from base	Tully Limestone	-0.7%
23	Leakoff Coefficient	Increase 10% from base	Upper Marcellus	-0.9%
47	Leakoff Coefficient	Increase 10% from base	Onondaga Limestone	-0.9%
20	Young's Modulus	Decrease 10% from base	Upper Marcellus	-1.3%
41	Horizontal Stress Gradient	Increase 10% from base	Onondaga Limestone	-2.1%
12	Young's Modulus	Decrease 10% from base	Hamilton Shale	-2.3%
34	Horizontal Stress Gradient	Decrease 10% from base	Lower Marcellus	-4.8%
18	Horizontal Stress Gradient	Decrease 10% from base	Upper Marcellus	-5.8%
26	Horizontal Stress Gradient	Decrease 10% from base	Cherry Valley	-6.3%
1	Horizontal Stress Gradient	Increase 10% from base	Tully Limestone	-7.4%
9	Horizontal Stress Gradient	Increase 10% from base	Hamilton Shale	-8.7%

Plan for Next Quarter

The current modeling study will be continued to develop and utilize a statistical methodology which will aim to reconcile discrepancies between numerical model fracture height and length calculations and microseismic cloud height and length estimates.

Topic 3 – Deep Subsurface Rock, Fluids, & Gas

Approach

The approach is to work across a broad spectrum of detailed geochemical and biogeochemical investigations that could have significant impact on completion and production.

Results & Discussion

Cole Lab (OSU)

Deliverable 1: Preparation of a manuscript that compares/contrasts the Lower Marcellus with Lower Point Pleasant.

Marcellus Characterization.

Work continues on quantifying the mineralogy of core samples from hydraulic fracturing targets in the Marcellus (**Figure below**) and Point Pleasant Formations. QEMSCAN (**below**) and BSE imagery aids mineral identification of trace phases in the fine silt and clay-sized fractions that are not detected with powder XRD. This effort will help determine and quantify minerals that solubilize to produce major and trace elements measured in produced fluids. Red box in the lower magnification image (**below, left**) outlines the zoomed-in image at right, in which trace phases (red pixels) are detected, including U-Ti oxides, TiO_2, REE phosphates, and barite. Some of these phases may incorporate elements that contribute to measurable radioactivity in produced fluids.

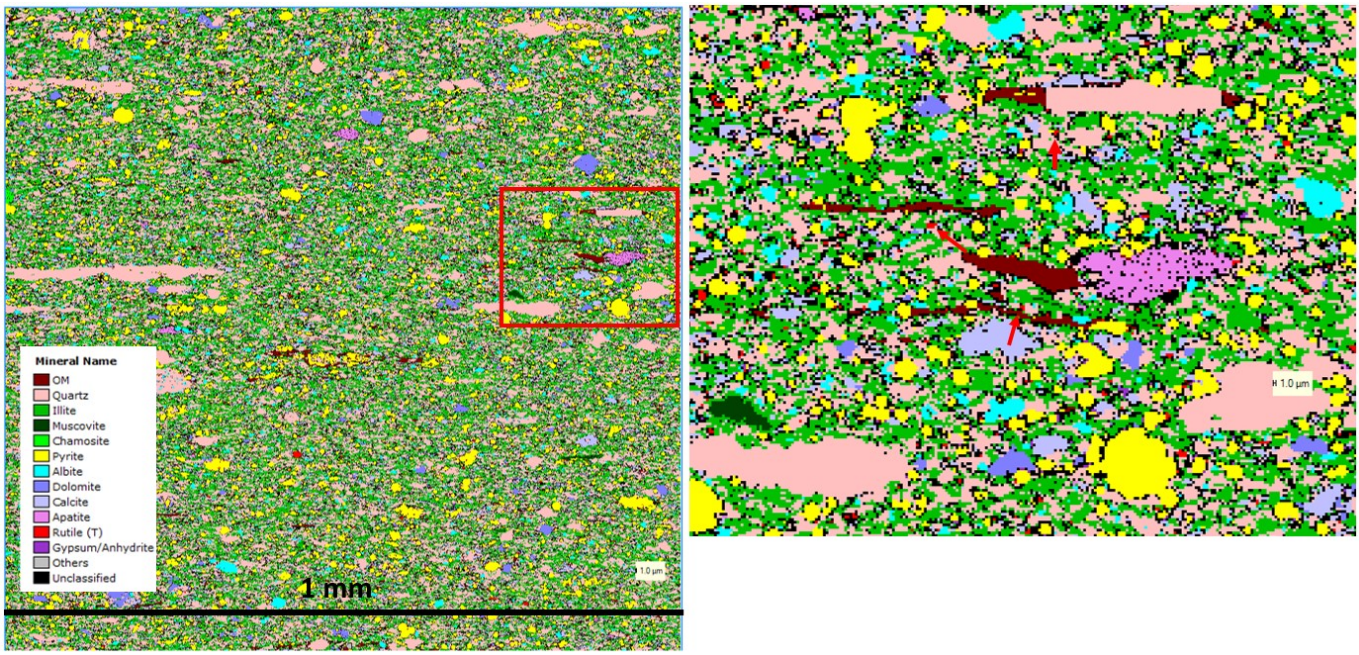

Fig. 3.1. QEMSCAN imagery of lower Marcellus core, depth 7543 feet. **Left:** 1 mm^2 region of polished core shows mineral replacement of organic matter (OM, brown) primarily by quartz (light pink), pyrite (yellow) and phosphate (bright pink). Clay sized fraction includes minerals of interest for potentially solubilizing REE and U (red pixels, arrowed).

Manuscript in preparation, to be submitted to *Geology*:

"Comparison of organic matter macerals and associated mineral matrices in hydraulic fracturing targets from the lower Marcellus and Point Pleasant Formations". J. Sheets, S. Welch, T. Liu, A. Swift, D. Cole)

Deliverable 2: Preparation of a manuscript that couples flowback geochemistry to the distribution of major and trace elements in a hydraulic fracturing target (Lower Marcellus), fluid and rock collected from the same well (MIP 3H).

Fluid Chemistry and Water-Rock Interaction.

Interpretation of flowback fluid geochemistry in concert with the formation geochemistry and mineralogy from both the MSEEL site and the Utica sites continues. We have a manuscript in prep from this work. The results of the water analysis show that the FP fluid compositions are remarkably similar in spite of the different lithology between the UPP and Marcellus formations. The strong correlations among most of the major constituents in the brines with conservative species such as Cl or Br, which suggests that in situ brine composition in these formations diluted by the relatively fresh input fluids used in hydraulic fracturing is overwhelmingly controlling flowback brine composition, and the large scale temporal changes can be described by diffusion of these brines in micropores to the larger fracture network generated by hydraulic fracturing (Balashov et al 2015). The Na-Cl-Br plot (Fig. 2) is consistent with the observations of Engle and Rowan (2014) which suggests the brines from both the UPP and Marcellus formation are derived from evaporated paleo-seawater. However, the small but systematic decrease in the Cl/Br ratio over time suggests a potential contribution from halite dissolution early on during.

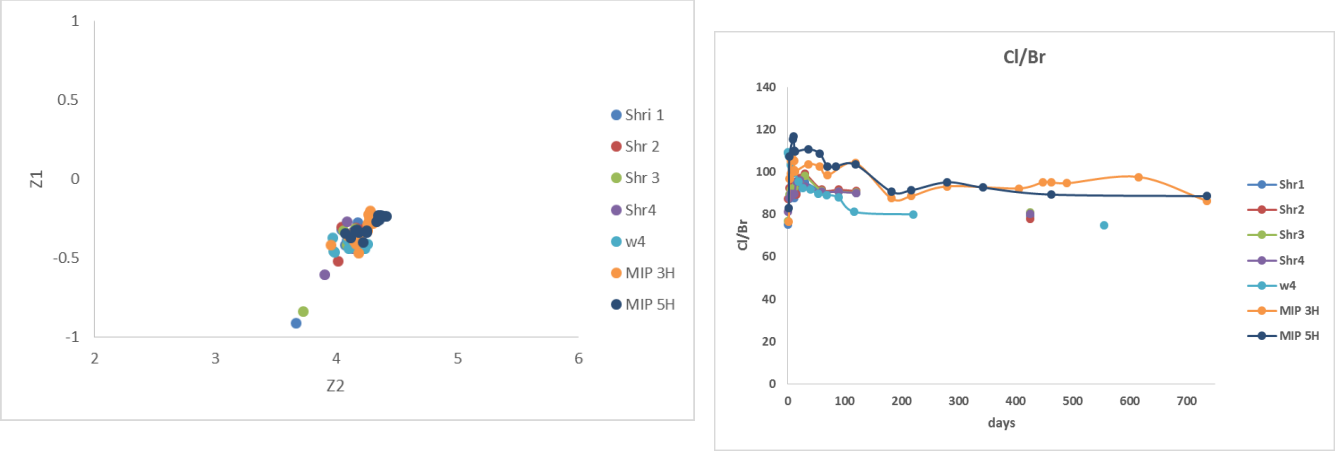

Figure 3.2. Left plot: (Na-Cl-Br) from flowback fluids from both the MSEEL site (MIP 3H and 5H) and the UPP wells (Shr 1-4 and W4).

However, there are distinct differences in the geochemistry of the brines that reflect geochemical processes that have occurred over geologic time, including dolomitization, sulfate reduction and ion exchange reactions as well as contemporaneous brine-rock interaction, either from the dissolution of primary rock, oxidation of reduced species or adsorption-desorption reactions in the subsurface. These differences are most apparent in the geochemistry of sulfur species and alkaline earth elements. In Figure 3.2, the data plot along a trajectory that is consistent with evaporated paleo seawater. Z1 is 1/sqrt2* ln(Na/Cl) ; Z2 is sqrt2/sqrt3 * ln ((sqrt(Na*Cl)/Br) Right plot: Cl/Br ratios in flowback brines.

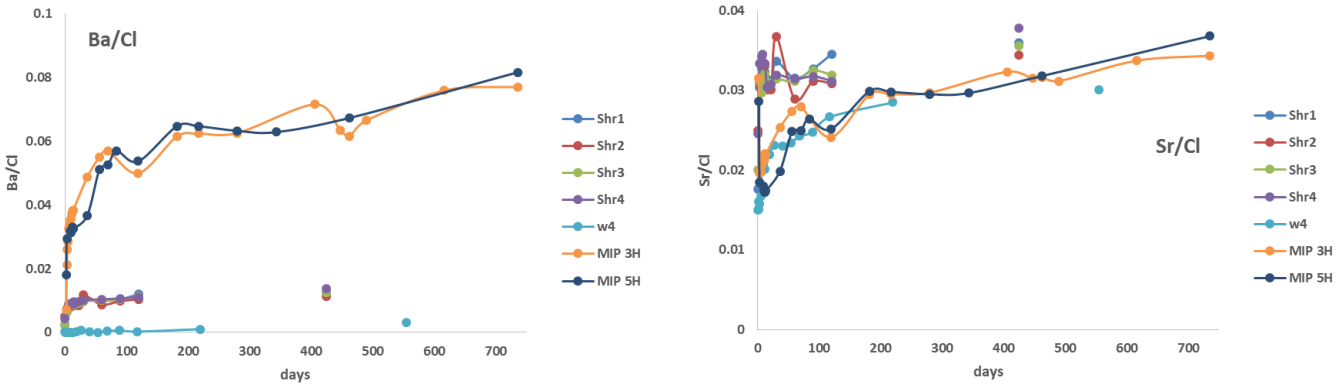

Figure 3.3. Left plot: Ba/Cl and Right plot: Sr/Cl ratios in flowback fluids from MSEEL and UPP wells showing and increase in the Ba/Cl and Sr/Cl ratios over time. The increase in alkaline earth elements compared to Cl reflects ion exchange reactions and dissolution of Sr and Ba bearing phases such as barite/celestite or gypsum, carbonates, or phosphate minerals.

Deliverable 2. Produce a draft of a manuscript comparing geochemistry of flowback fluids between Utica and Marcellus wells.

Manuscript in preparation for *ES&T* journal:

"Flowback fluid signals from the Appalachian Basin: Focus on the Marcellus and Utica-Point Pleasant". Susan A. Welch, Julia M. Sheets, Rebecca A. Daly, Andrea J. Hanson, **more authors** and David R. Cole

References:

Balashov, VN, Engelder T, Gu X, Fantle MS, and Brantley SL, 2015, A model describing flowback chemistry changes with time after Marcellus Shale hydraulic fracturing. AAPG Bulletin, 90, 143-154.

Engle MA, and Rowan EL, 2014, Geochemical evolution of produced waters from hydraulic fracturing of the Marcellus Shale, northern Appalachian Basin, A multivariate compositional data analysis approach. International Journal of Coal Geology, 126, 45-56.

Darrah Lab (OSU)

Milestone 1. Characterization of changing gas composition throughout production history.

Deliverable 1. Submit manuscript about changing gas composition throughout production history.

Update: Plan to circulate manuscript draft by 9/1/2019.

Manuscript entitled: The changing composition of hydrocarbon and noble gases during the early production of a Marcellus Shale Gas Well; Authors: T. Darrah, C.J. Whyte, D. Cole, S. Sharma, and T. Carr; Planned submission to Geochimica et Cosmochimica Acta

Milestone 2. Characterization of hydrocarbon generation/residence time.

Deliverable 2. Submit manuscript about hydrocarbon residence time for Marcellus production gas.

Update: Plan to circulate manuscript draft by 10/15/2019.

Manuscript entitled: Determining the residence time of natural gas produced from the Marcellus Shale using radiogenic noble gas isotopes. Authors: T. Darrah, C.J. Whyte, B. Lary, D. Cole, S. Sharma, and T. Carr; Planned submission to Geochimica et Cosmochimica Acata

Milestone 3: Characterize the radiogenic noble gas composition of Marcellus and adjacent formation fluid inclusions and solids.

Deliverable 3. Complete analyses; process data; submit report by 9/15/2019.

Update: Remaining analyses in progress (n=14).

Sharma's Lab

1. Experiments to understand kerogen-frac fluid and interaction. We continue to conduct high temperature and pressure shale-frac fluid interaction experiments to isolate the effects of maturity and fracturing fluid composition on functional groups and kerogen molecular structure. The extraction of kerogen from some of these samples is complete and and some experiments are currently underway.

Heterogeneities present in kerogen molecular within a particular kerogen type and maturity could affect the shale-frac fluid interactions. To understand such heterogeneities, kerogen molecular structure from Marcellus shale was compared with the molecular structure of other shale samples with similar type and maturity. Our results indicate that even within a particular kerogen type and maturity, the molecular structure of kerogen in different shale formations can be drastically different. We demonstrated that the molecular simulation models currently used to determine fluid flow and sorption of hydrocarbons (and fracturing fluids) do not incorporate such heterogeneities. Therefore, for more efficient HC and fracturing fluid recovery, there is a critical need to better design fracturing fluids and molecular simulation models accounting for kerogen structural heterogeneities. We have submitted these finding to the journal *Nature Materials*.

Deliverables:

- Submitted a manuscript to the journal *Nature Materials*.
- Analyze and interpret data from ^{13}C NMR analysis by Fall 2019.

2. Understanding the type, amount and origin of the gas. Results from the open and closed pyrolysis experiments are being compiled in a manuscript by V. Agrawal. The novel findings of the experiments indicate that the pyrolysates on maturation generally evolves from Paraffinic-Aromatic-Naphthenic (P-N-A) low wax to gas condensate petroleum type. Using MSSV-Py-GC, we evaluated the "late gas" generation potential by determining the gas yields at higher temperatures (560 ^{o}C and 700 ^{0}C). It was observed that the late gas potential increases with maturity up to 2.0% VRo to roughly 40 mg/g TOC and then decreases again during metagenesis due to late methane generation. Since the traditional source rock evaluation is based on open-system pyrolysis screening-methods which does not incorporate the late gas potential, our results demonstrate that the previous estimations on Marcellus shale reserves can be underestimated.

Deliverables:

- Submitted an abstract for ES-AAPG 2019, Columbus, OH.
- Submit a manuscript to the journal *Fuel* by Fall 2019.

3. Microbial lipid analysis of sidewall cores from MSEEL: Ph.D. student Rawlings Akondi is currently responding to reviewer comments on the manuscript that was submitted to Frontiers in Microbiology. The manuscript examines the distribution of membrane lipid biomarkers in the side wall core samples collected from the MSEEL well and the WV 6 core samples collected and stored under surface ambient conditions. In accordance with the reviewers comments, we have included additional PLFA data from experiments that were performed using strains of isolated Halanaerobium congolense bacterium cells. The Halanaerobium cells were cultured under pressurized conditions of 0.1 Mpa, 21 MPa, 35MPa, and 48 MPa (Booker et al., 2019). Stress indicative biomarkers like oxiranes, keto, and dimethyl lipid biomarkers were only present in the subsurface MSEEL core samples. There were, however, no oxiranes, dimethyl, and keto lipid biomarkers in the surface-stored WV 6 core samples. Similar to our results, Booker et al. (2019) also observed higher relative abundance of the oxiranes and keto in the samples cultured under subsurface pressurized conditions of 48 MPa compared to the cells cultured under lower pressure growth conditions of 0.1 MPa. This observation in combination with our results suggest that the oxiranes, keto, dimethyl esters may be linked with microbial adaptation for survival under pressurized stressed conditions. On the other hand, the absence of the stress biomarkers after storage in WV 6 core samples could suggest the transformation of the subsurface adapted biomarkers to relatively more stable structures in response to low temperatures and pressures in the surface. We also observed higher ratios of Gram (+), saturates:unsaturates, and trans/cis biomarkers in the MSEEL core samples, reflecting higher pressure conditions associated with the subsurface. Similarly, there was a corresponding increase in the ratio of saturate:unsaturate and the trans/cis lipid biomarkers with increasing pressure. Halanaerobium samples cultured under pressure conditions of 48 MPa had the highest saturate:unsaturated and trans:cis ratios compared to the samples cultured under lower pressured samples (0.1 MPa, 21 mPA, and 35 MPa). Oxiranes, keto, and dimethyl esters

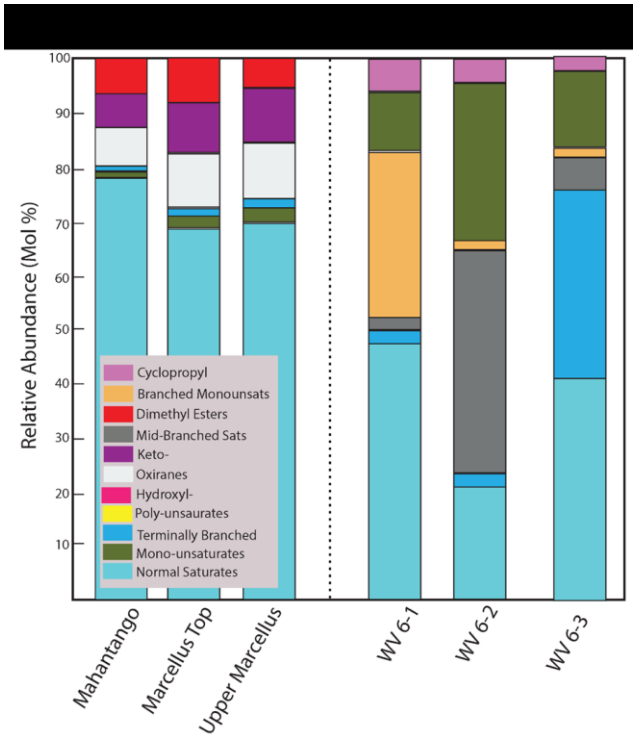

Figure 3.4. Relative abundance and distribution of PLFA biomarker functional groups for the MSEEL and WV 6 core samples. MSEEL-1 and WV 6-1=Mahantango, MSEEL-2 and WV 6-2=Marcellus Top, MSEEL-3 and WV 6-3=Upper Marcellus Shale zones. The cores from the same well had similar distribution of lipid communities.

are associated with membrane bulking, adaptations which could be important for membrane intergrity under high pressure conditions.

Deliverables:

- Ph.D student, Rawlings Akondi has successfully defended his dissertation titled "Utilizing Lipid Biomarkers to Understand the Microbial Community Structure of Deep Subsurface Black Shale Formations".
- Submitted an abstract to the GSA 2019 Annual Meeting in Phoenix, Arizona

PUBLICATIONS & PRESENTATIONS

1. Agrawal, V., and S. Sharma, (2019), Pitfalls in modeling physicochemical properties of shales using kerogen type: Nature Materials (*in review*).
2. Akondi, R., Sharma S., Texler, R., Pfifnner S. (2019). Effects of Sampling and Long Term Storage on Microbial Lipid Biomarker Distribution in Deep Subsurface Marcellus Shale Cores. Frontiers in Microbiology *(in review)*.
3. Sharma S., Agrawal, V., Akondi, R. (2019) Role of Biogeochemistry in Efficient Shale Oil and Gas Production. Fuel *(in review)*.
4. Agrawal, V., S. Sharma, N. Mahlstedt 2019, Determining the type, amount and kinetics of hydrocarbons generated in a Marcellus shale maturity series. Eastern Section AAPG 48th Annual Meeting in Columbus, OH.

Plan for Next Quarter

Project Title	Milestone Name	Milestone Description	Estimated Completion Date
Marcellus Shale Energy and Environment Laboratory (MSEEL)	Complete laser ablation inductively coupled plasma mass spectrometry (ICP-MS) analysis on polished thick section of hydraulic fracturing target (Lower Marcellus) to track distribution of trace elements in the rock. (Cole)	Draft manuscript nears completion that compares/contrasts the Lower Marcellus with Lower Point Pleasant. The paper is entitled: "Comparison of organic matter macerals and associated mineral matrices in hydraulic fracturing targets from the lower Marcellus and Point Pleasant Formations". J. Sheets, S. Welch, T. Liu, A. Swift, D. Cole) To be submitted to *Geology*	9/30/2019
Marcellus Shale Energy and Environment Laboratory (MSEEL)	Complete assessment of comparison of Marcellus and Utica flowback fluids (Cole)	A manuscript nears completion entitled: "Flowback fluid signals from the Appalachian Basin: Focus on the Marcellus and	9/30/2019

		Utica-Point Pleasant". Susan A. Welch, Julia M. Sheets, Rebecca A. Daly, Andrea J. Hanson, more authors and David R. Cole To be submitted to *ES&T*	
Marcellus Shale Energy and Environment Laboratory (MSEEL)	Characterization of water and gas samples for noble gas (Darrah)	Manuscript entitled: The changing composition of hydrocarbon and noble gases during the early production of a Marcellus Shale Gas Well; Authors: T. Darrah, C.J. Whyte, D. Cole, S. Sharma, and T. Carr; Planned submission to Geochimica et Cosmochimica Acta	9/1/2019
Marcellus Shale Energy and Environment Laboratory (MSEEL)	Characterization of fluid inclusion gas compositions for noble gas and hydrocarbons. (Darrah)	Complete analyses; process data; submit report by 9/15/2019. Update: Remaining analyses in progress (n=14).	9/15/2019
Marcellus Shale Energy and Environment Laboratory (MSEEL)	Submit manuscript about hydrocarbon residence time for Marcellus production gas. (Darrah)	Manuscript entitled: Determining the residence time of natural gas produced from the Marcellus Shale using radiogenic noble gas isotopes. Authors: T. Darrah, C.J. Whyte, B. Lary, D. Cole, S. Sharma, and T. Carr; Planned submission to Geochimica et Cosmochimica Acata	10/30/2019

Topic 4 – Produced Water and Solid Waste Monitoring –

Approach

MIP Site

Over three years into the post completion part of the program, the produced water and solid waste component of MSEEL has continued to systematically monitor changes in produced water quality and quantity. During year one of the study, hydraulic fracturing fluid, flowback, produced water, drilling muds and drill cuttings were characterized according to their inorganic, organic and radio chemistries. In addition, surface water in the nearby Monongahela River was monitored upstream and downstream of the MSEEL drill pad. Toxicity testing per EPA method 1311 (TCLP) was conducted on drill cuttings in both the vertical and horizontal (Marcellus) sections to evaluate their toxicity potential. Sampling frequency has been slowly scaled back following well development. **Error! Reference source not found.** 4.1 shows an "X" for sample collection dates. Wells 4H and 6H were brought back online in late 2016. Other blank sample dates in Table 4.1 indicate that samples were not collected, due to lack of availability of produced water from the well(s).

Table 4.1: MIP sampling events are indicated with an "X".

Year	2015			2016												
Day/Month	10-Dec	17-Dec	22-Dec	6-Jan	20-Jan	3-Feb	2-Mar	23-Mar	20-Apr	18-May	2-Jul	17-Aug	21-Jun	19-Oct	16-Nov	14-Dec
3H	X		X	X	X	X		X	X	X	X	X	X	X		X
4H															X	X
5H	X	X	X	X	X	X	X	X	X	X	X	X	X	X	X	
6H															X	X

Year	2017									2018					
Day/Month	13-Jan	14-Feb	13-Mar	7-Apr	5-May	12-Jul	20-Dec	3-Nov	20-Dec	22-Jan	23-Feb	16-May	2-Aug	16-Oct	15-Dec
3H	X	X	X	X	X	X	X	X	X	X	X	X	X		X
4H	X	X	X	X	X					X	X	X	X	X	X
5H		X			X				X	X		X		X	X
6H	X	X	X	X	X							X	X		

Year	2019	
Day/Month	24-Jan	5-Mar
3H	X	X
4H	X	X
5H	X	X
6H		X

Boggess Site

Two control wells; 9H and 17H were selected for solids and aqueous studies at the newly developed Boggess well site. Tophole was completed in Feb 2019 for 9H and Jan 2019 for 17H. Samples of vertical drilling were not obtained due to completion prior to the start of the Boggess project.

Horizontals were initiated on 19 June 2019 for 17H and 20 May 2019 for 9H Table 4.2. A drilling mud sample along with depth samples at 8,500; 10,000; 11,000; 13,000; and 15,000 were collected and analyzed for parameters shown in Table 4.3.

Table 4.2. Sample depth and dates for collection of horizontal drilling mud and cutting samples.

Depth	Mud 9H	8500 9H	10000 9H	11000 9H	13000 9H	15000 9H
Date	5/27/2019	5/27/2019	5/28/2019	5/29/2019	5/29/2019	5/30/2019

Table 4.3. Solids analysis list.

Analysis	Method	Units	Parameter
Diesel Range Organics by GC-FID	SW8015M	mg/Kg-dry	DRO (C10-C28)
			ORO (C28-C40)
		% Rec	Surr: 4-terphenyl-d14
Gasoline Range Organics by GC-FID	SW8015D	ug/Kg	GRO C6-C10)
		% Rec	Surr: Toluene-d8
Volatile Organic Compounds	SW8260B	ug/Kg-dry	Ethylbenzene
			m,p- Xylene
			o- Xylene
			Styrene
			Toluene
			Xylenes total
		% Rec	Surr: 1,2- Dichloroethane-d4
			Surr: 4-Bromofluorobenzene
			Surr: Dibromofluoromethane
			Surr: Tolouene-d8
Radionuclides	EPA 901.1	pCi/g	Potassium-40
			Radium-226
			Radium-228
	9310		Gross Alpha
			Gross Beta
Inorganics	SW9056A	mg/Kg-dry	Br
			Cl
			SO4
	SW9034		sulfide
	E353.2		nitrate
	E354.1		nitrite
	A2510M	µS/cm	EC
	SW9045D	units	pH
	A4500-CO2 D	mg/Kg-dry	alk bicarb
			alk carb
			alk t
	E365.1 R2.0		TP
	SW6020A		Ag
			Al
			As
			Ba
			Ca
			Cr
			Fe
			K
			Li
			Mg
			Mn
			Na
			Ni
			Pb
			Se
			Sr
			Zn
Moisture	E160.3M	%	Moisture
Chemical Oxygen Demand	E4104 R2.0	mg/Kg-dry	COD
Organic Carbon - Walkley-Black	TITRAMETRIC	% by wt-dry	OC-WB
Oil & Grease	SW9071B - OG	mg/Kg-dry	O&G

Results & Discussion

MIP Site

Major ions – trends in produced chemistry

While makeup water was characterized by low TDS (total dissolved solids) and a dominance of calcium and sulfate ions, produced water from initial flowback is essentially a sodium/calcium chloride water (**Figure 4.1**). While produced water TDS (total dissolved solids) increased by an order of magnitude from initial flowback to the present, the ionic composition of produced water changed very little through 1281 days post completion. Produced water TDS was affected by shut-in/turn-in cycles at individual wells. For example, upon turn-in TDS was invariably very low but reached pre-shut-in concentrations within a month. MIP 3H was shut-in sometime after day 966 and turned back in just prior to sampling on day 1101. While concentrations are magnitudes lower, the proportion of ionic compounds is consistent with previous samples

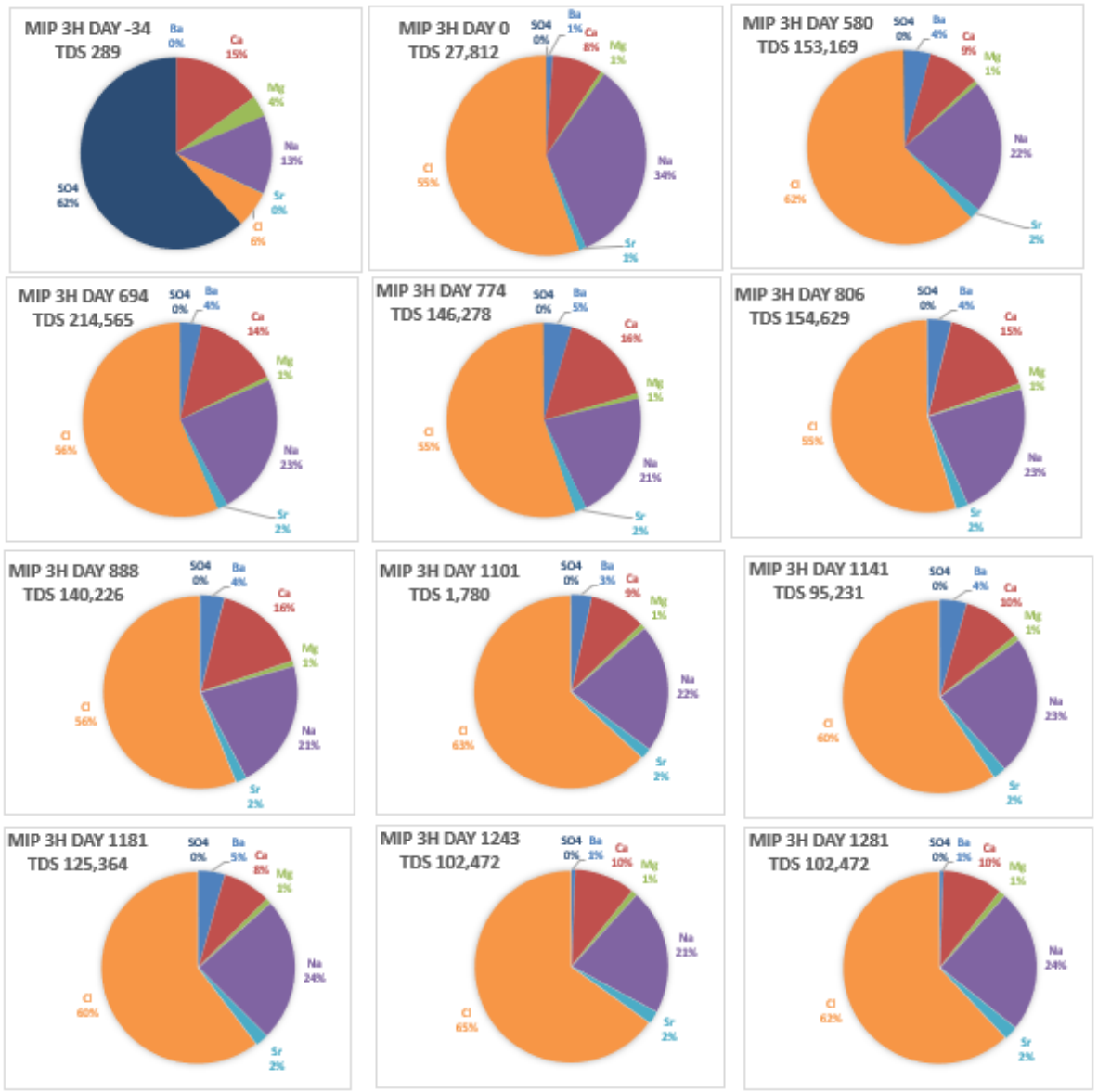

Figure 4.1. Changes in major ion concentrations in produced water from well MIP 3H. Top left Day -34

represents makeup water from the Monongahela River, top center is produced water on the first day (Day 0) and the remainder of pie charts show flowback and produced water on sampling dates through the 1181th day post completion.

In wells 3H and 5H, TDS increased rapidly over the initial 90 days post completion while TDS stabilized between 100,000 and 200,000 mg/L through day 1181(3H) (Figure 4.2). Note that 3H and 5H were both shut-in near day 966 and brought back online prior to sampling on day 1101. 3H and 5H are showing an upward trend following day 1101.

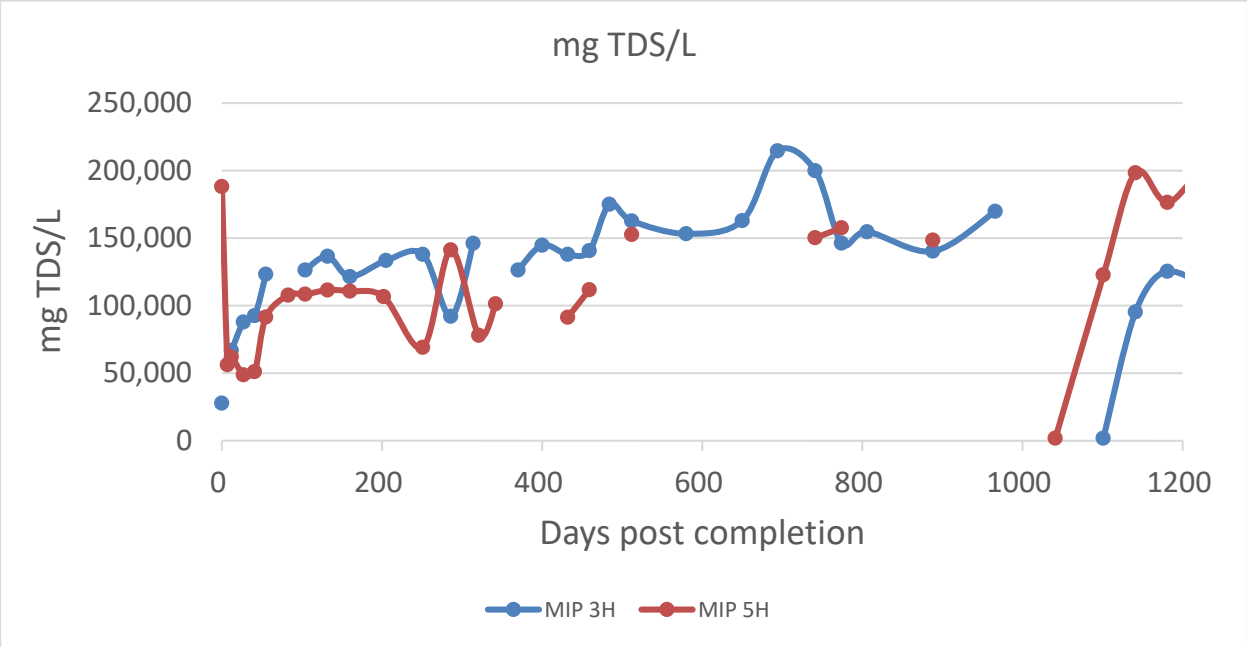

Figure 4.2. Changes in produced water TDS sdc (sum of dissolved constituents) through the first 1181 days post completion (3,5H).

The older 4H and 6H wells offer insight into the longer-term TDS trend. Those wells only came back on line during this quarter after a shut-in period of 315 days and those results vary but they are much lower than the current values for wells MIP 3H and 5H. Both 4H and 6H were shut down during late 2017. TDS was very low at MIP 4H during the first sampling event of early 2018. Calculated TDS was 2,455 mg/L and lab reported TDS was 2,300 mg/L. A similarly low TDS trend was noted when well 4H went back online around 1,793 days post-completion (after being shut-in for 315 days) and again when 6H went online around day 2,417 A rise in TDS subsequently follows the initial return to online status with TDS on an upward trend, reaching 160,000 for 6H. MIP 6H has been offline during this quarter's sampling events. MIP 4H is on a downward trend after peaking at around 140,000 at day 2552 (Figure 3). 4H and 6H were not sampled during this reporting period.

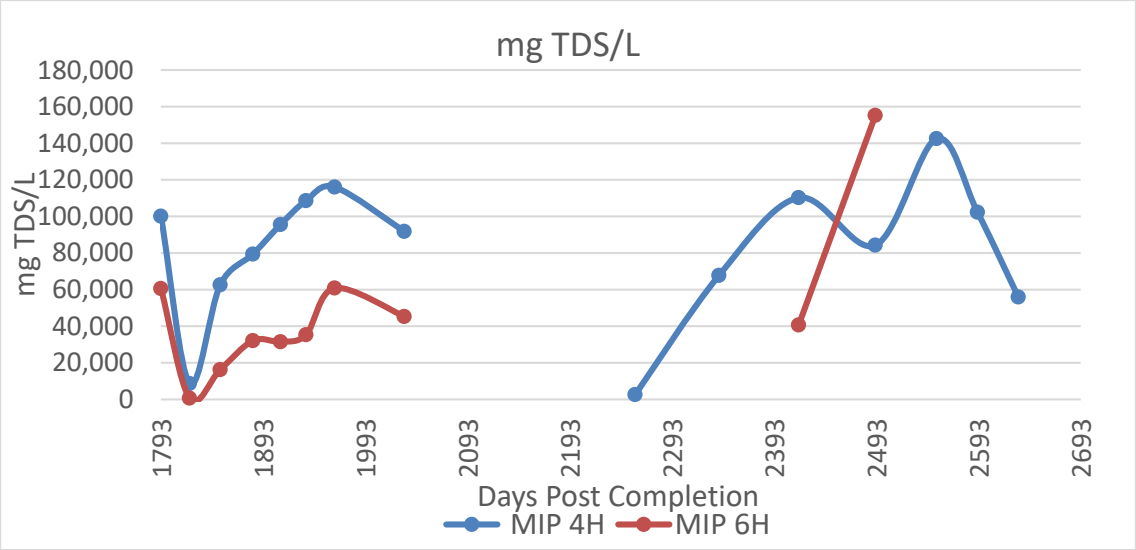

Figure 4.3. Changes in produced water TDS sdc (sum of dissolved constituents) through the days 1793 to 2632 post completion (4,6H).

Water soluble organics

The water soluble aromatic compounds in produced water: benzene, toluene, ethylbenzene and xylene were never high. With two exceptions at post completion day 321 and 694, benzene has remained below 30 µg/L (Figure 4.4). This seems to be a characteristic of dry gas geologic units. After five years, benzene has declined below the drinking water standard of 5 µg/L.

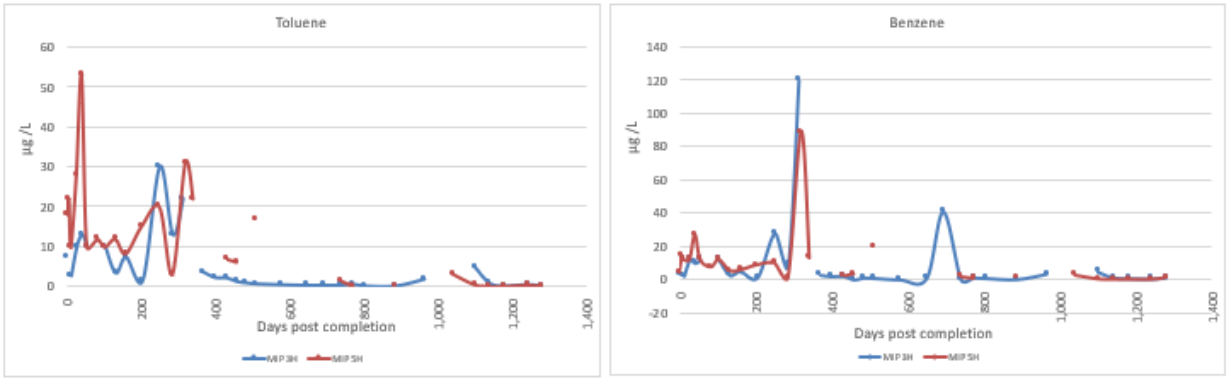

Figure 4.4. Changes in benzene and toluene concentrations. The figure shows data from well both 3H and 5H.

Radium isotopes

The radiochemical concentrations were determined by Pace Analytical in Greensburg PA, a state certified analytical lab. Radium concentrations generally increased through 800 days post completion at wells MIP 3H and 5H. Maximum levels of the radium isotopes reached about 21,800 pCi/L at the unchoked 3H well and around 17,800 5H. After returning online prior to day 966, both wells are on a general upward trend through the most recent sampling event, except for 3H on day 1101. (Figure 4.5).

Radioactivity in produced water

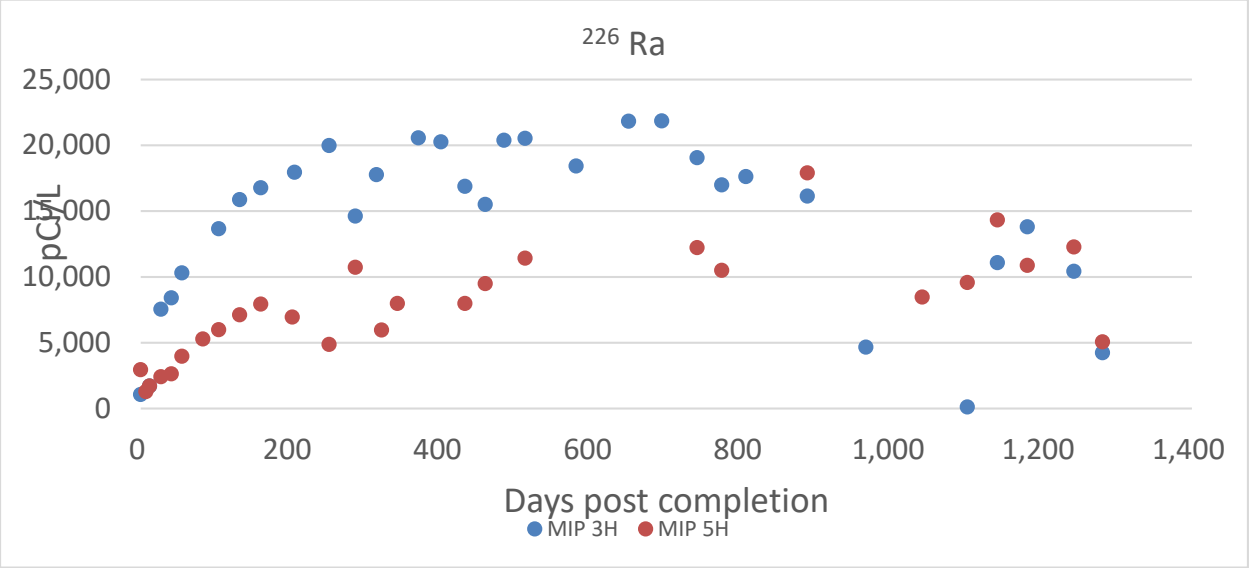

Figure 4.5. The radium isotopes are plotted against days post well completion. Well 5H was choked more periodically the 5H. 3H produced less water and lower concentrations of radium.

Radium concentrations at wells 4H and 6H were below 9,000 pCi/L during all sampling periods. Both wells were choked at day 1963. Well 4H was reopened at day 2225, radium was 58 pCi/L on the first sampling after the reopening and 3719 pCi/L at day 2257, a month later (Figure 4.6) peaked at 5,127 pCi/L then returned to 3,892 pCi/L. The same trend is noted at day 2492 when 4H returned online with 57 pCi/L then peaked at day 2632 with 8,197 pCi/L. Additional data is needed to capture long-term trends. 4H and 6H were not sampled during this reporting period.

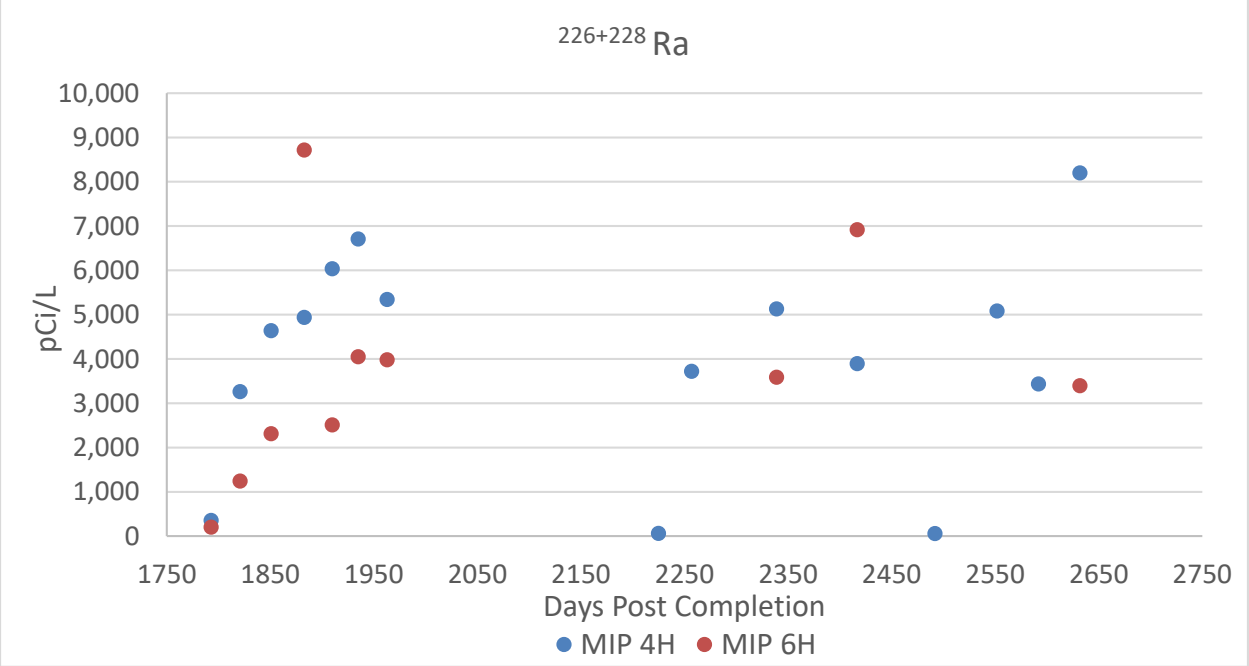

Figure 4.6. The radium isotopes are plotted against days post well completion. Well 4H and 6H were choked at day 1963. At day 2225, 4H was reopened showing a value of 58 pCi/L and reopened again at day 2492 showing a value of 57 pCi/L**.**

Figure 4.7 and 4.8 show the relationship between gross alpha and ^{226}Ra at 3H and 5H.

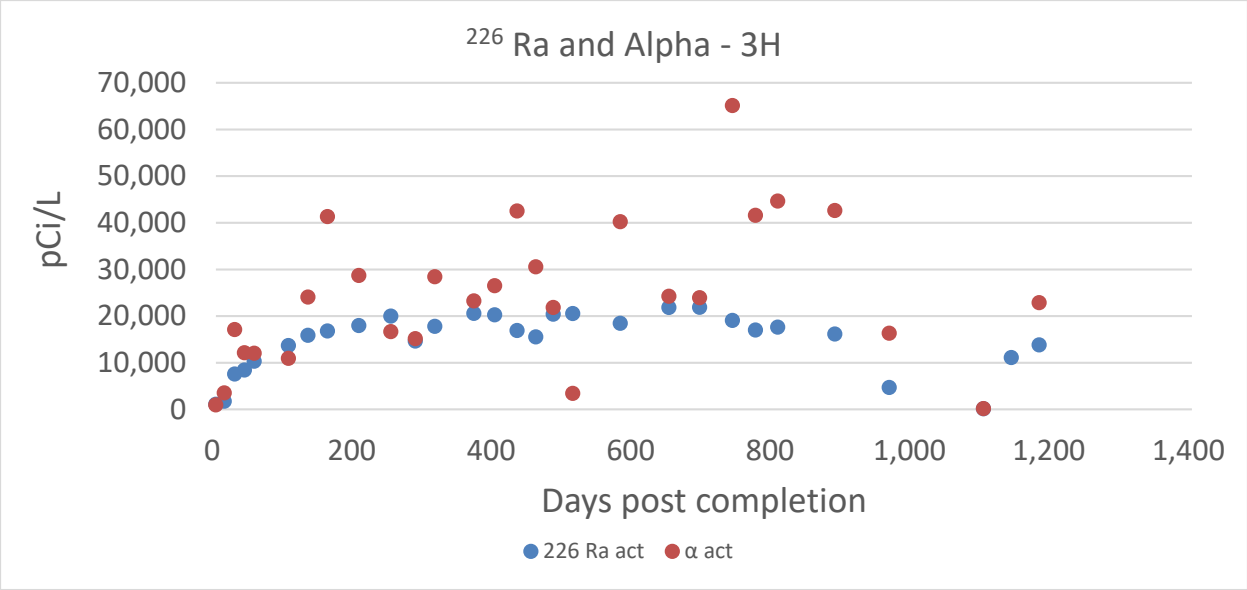

Figure 4.7. The relationship between gross alpha and ^{226}Ra as a function of time post completion at 3H.

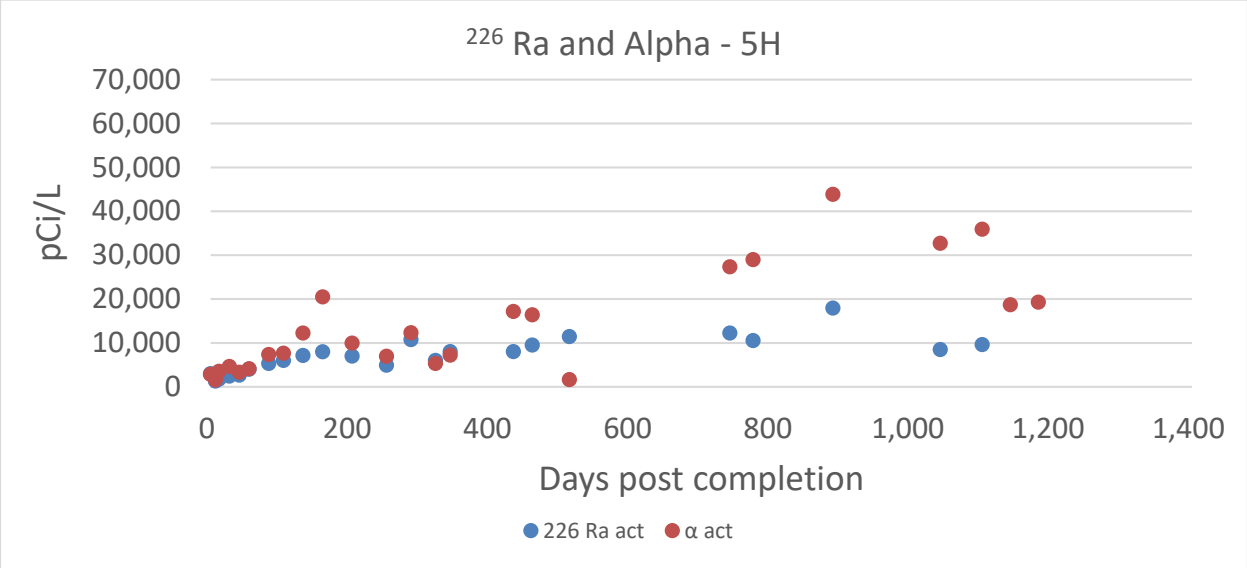

Figure 4.8. The relationship between gross alpha and ^{226}Ra as a function of time post completion at 5H.

The highest values reported in the older wells at 4H and 6H were 17,550 pCi/L gross alpha and 8,197 pCi/L ^{226}Ra. The relationship between gross alpha and ^{226}Ra for wells 4H and 6H are shown in Figure 4.9 and 4.10. 4H and 6H were not sampled during this reporting period.

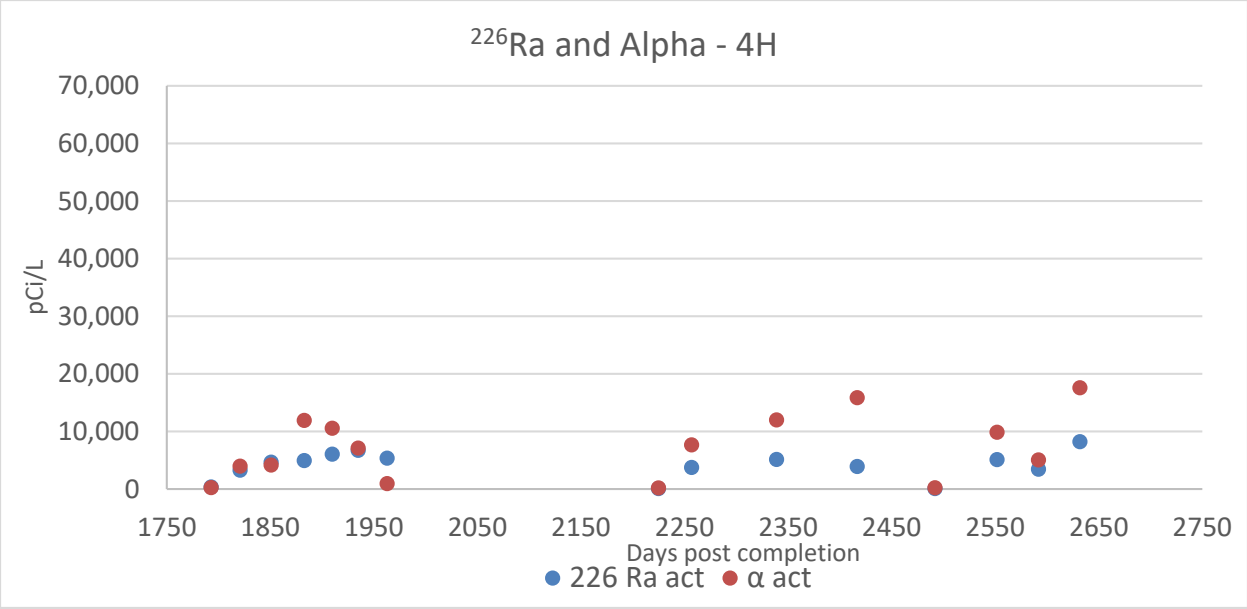

Figure 4.9. The relationship between gross alpha and ^{226}Ra as a function of time post completion at 4H.

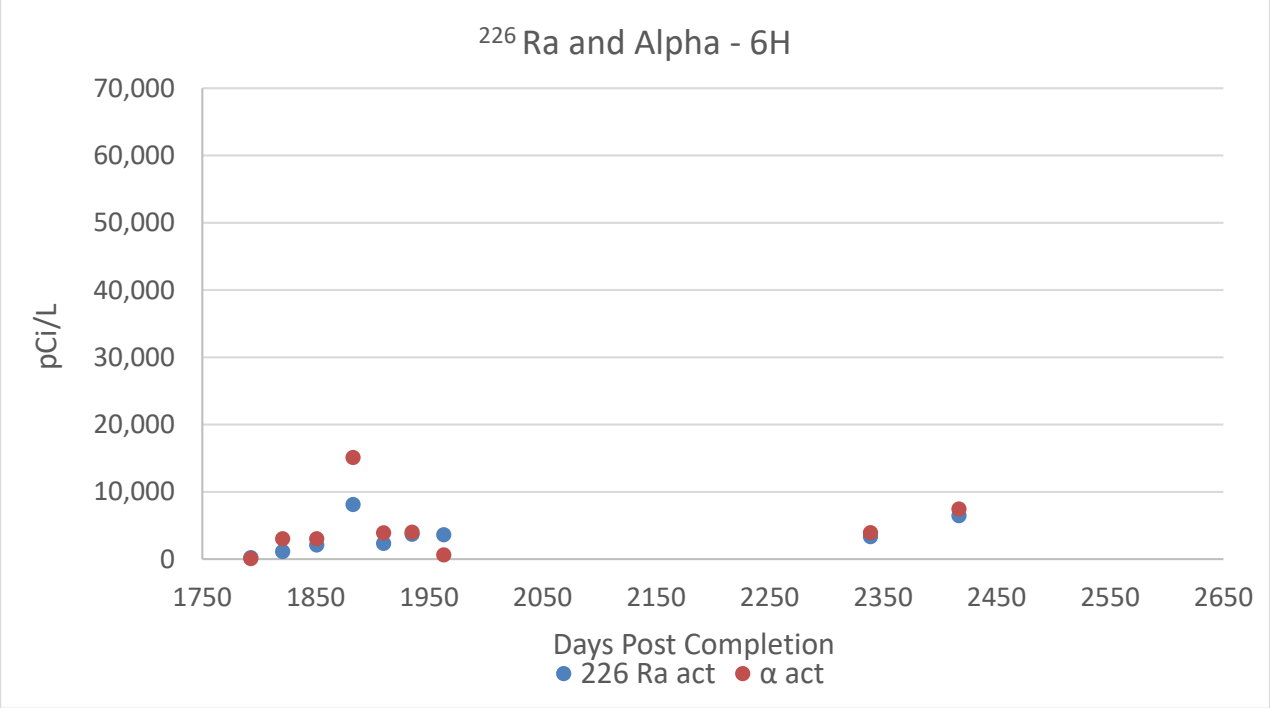

Figure 4.10. The relationship between gross alpha and ^{226}Ra as a function of time post completion at 6H.

Boggess Well

Analytical results have been received for drilling muds and cuttings collected at 9H. We are waiting on results for samples collected at 17H. Anions (Cl. SO4) and Cations (Ba, Ca, Mg, Mn, Na, and Sr) are shown in Figure 4.11. Drill cuttings are predominately Calcium.

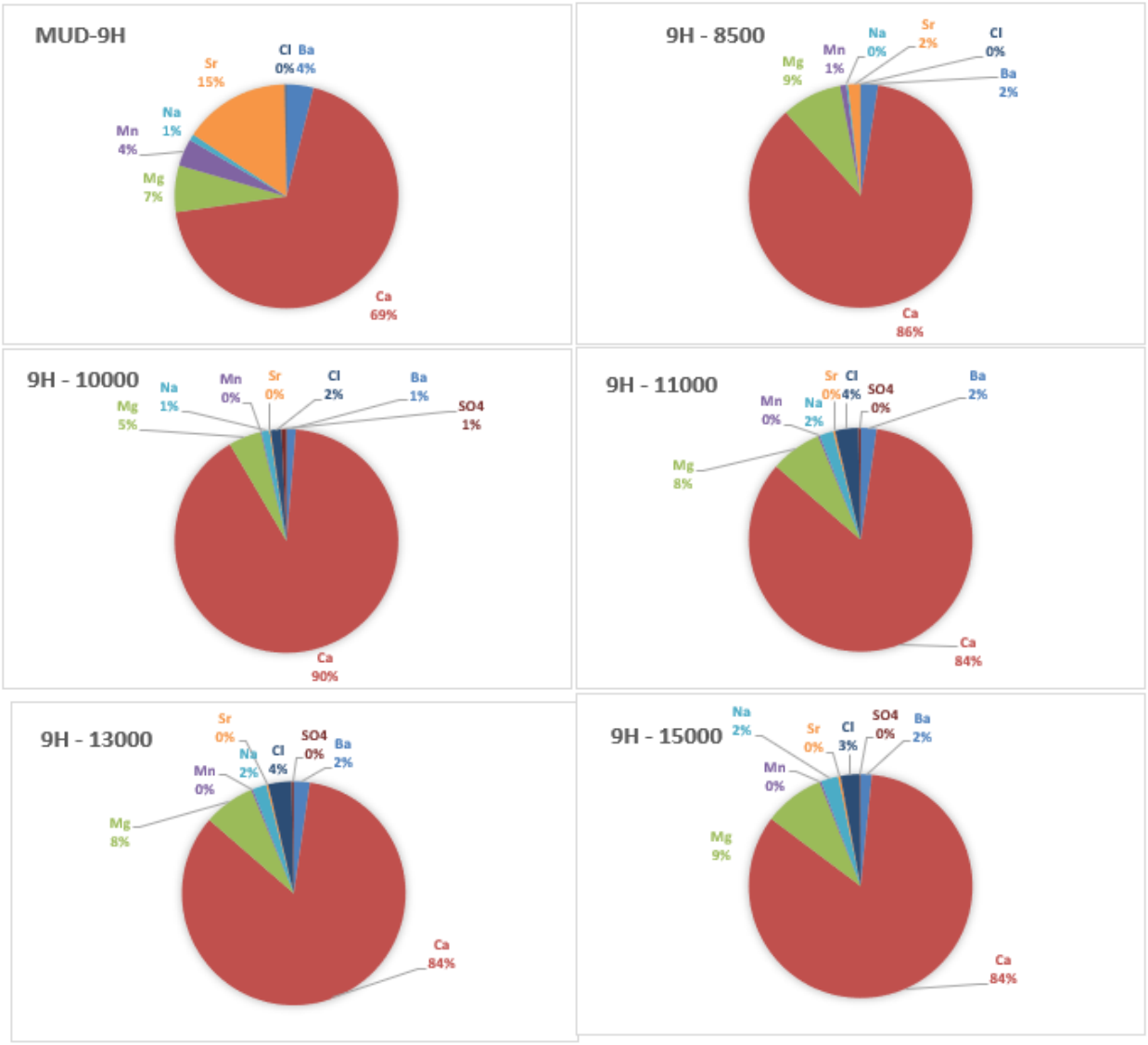

Figure 4.11. Anions/cations of drilling mud and cutting from 9H.

Figure 4.12 depicts combined radium 226 and 228 of solids in drilling mud and cuttings from 9H.

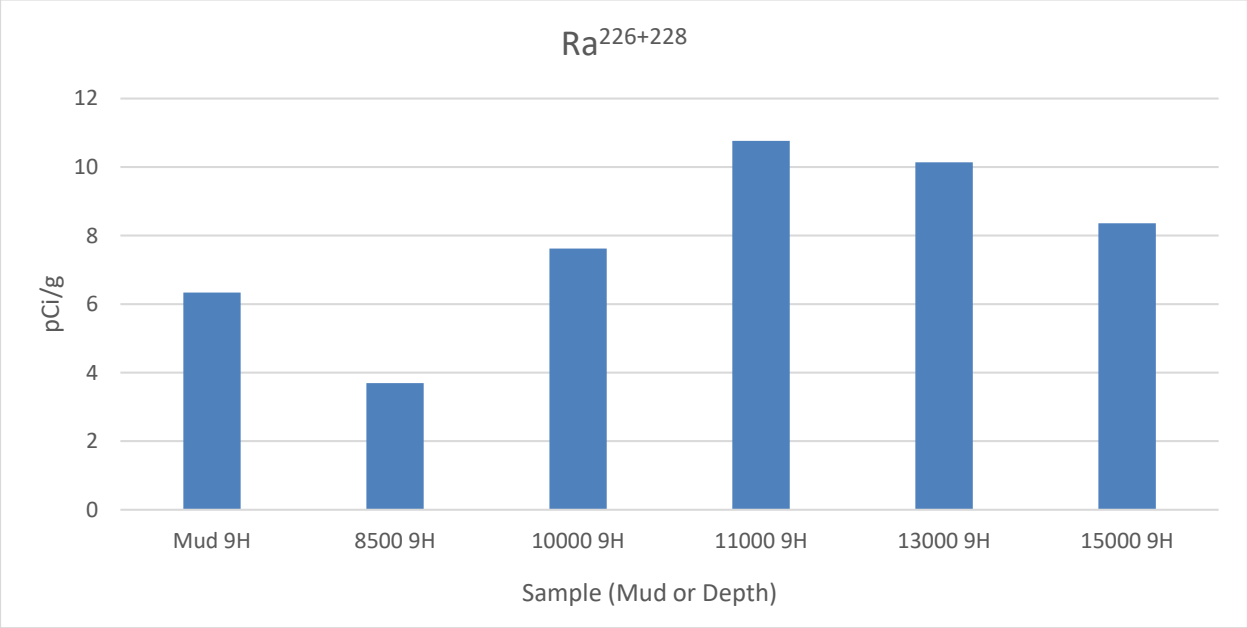

Figure 4.12. 9H Combined radium 226 and 228 for drilling mud and cuttings.

For comparison purposes, MIP 5H and 3H are shown in Figure 4.13

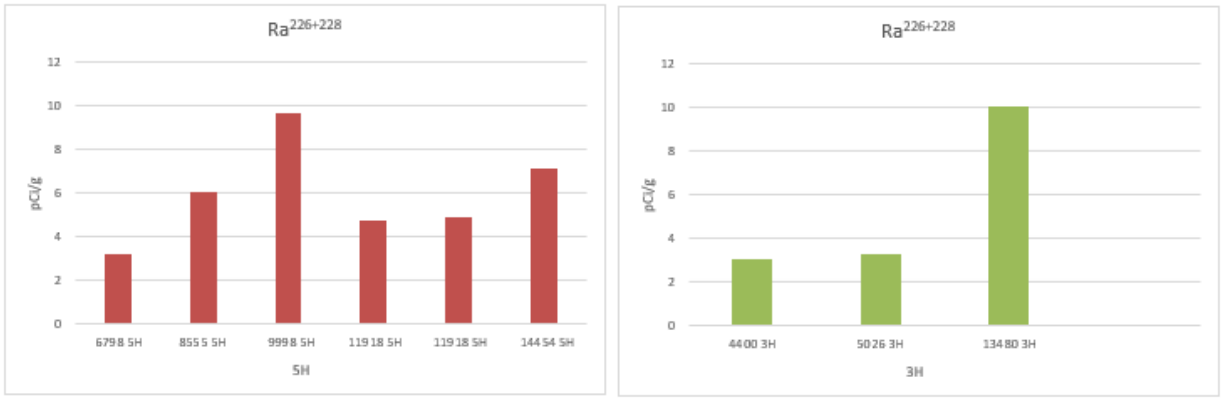

Figure 4.13. Combined Ra 226 + 228 for 5H and 3H MIP sites.

Products

None for this quarter.

Plan for Next Quarter

We will continue monthly sampling and analyze flowback/produced water (FPW) from MIP 3H, 4H, 5H and 6H if they are online.

We will continue sampling at Boggess Pad control wells 9H and 17H. Plans include collection of hydraulic fracturing fluid, flowback/produced water. Following the same protocols used at MIP wells, we will characterize their inorganic, organic and radio chemistries.

Topic 5 – Environmental Monitoring: Air & Vehicular

Approach

During this quarter the CAFEE team completed their 10th and 11th audit of the first MSEEL site. During the last update, we reported that the eddy-covariance system had been completed. Currently, the system has been deployed at the WVU Reedsville Farm where Mr. Dakota Oliver (DOE/NETL funded) has been working with Mr. Robert Heltzel (NSF Funded) to complete baseline and controlled release experiments. The controlled release rates are being conducted with 98-99% pure methane bottles connected to a manifold and mass flow controller. Three flow rates are targeted based a on a review of literature (Rella et al., Robertson et al., EPA/Brantley, Albertson et al., the EDF studies, and the ARPA-E Monitor targets). These rates include ~5, 10, and 20 standard liters per minute (SLPM). The distances were selected to be 50, 100, and 150 meters (m) from the complete OTM/eddy-covariance tower. Initial data have been analyzed and repeated runs are occurring now. This should mean that the installation of the system at the MSEEL 1.0 site should be completed by the target deadline of September 2019. Mr. Oliver also defended his master's thesis entitled, "Implications of Sampling Methods on Geospatial Mapping of Methane Sources." This work focused on comparison of the open-path analyzer (LI-7700 – 10 Hz) purchased as part of MSEEL and the previously acquired closed-path analyzer (UGGA – 1 Hz). As part of the NSF project and Dr. Johnson's start-up package a new high-frequency (5 Hz) methane and ethane analyzer has been ordered and will be added to the direct quantification system for subsequent audits. A new master's student, Mr. Diego Dranuta, has finished onboarding and is completing all safety and internal system training prior to Mr. Oliver's departure. Mr. Dranuta is currently examining the modifications necessary to the CAFEE telemetry system for data collection during energy audits based on drilling activity from MSEEL 2.0, see Figure 5.1.

Figure 5.1: Baseline Telemetry System to be Modified for Energy Audits.

Results & Discussion

Figure 5.2 shows the results of the latest MSEEL 1.0 methane emissions audits. The emissions from the site have returned to a lower level compared to the October and December (7th and 8th) audits. Note that these audits occurred after an enclosed gas processing unit (EPGU) was replaced. The cause of the excessive emissions (7th Audit ~43 kg/hr, 8th Audit ~8 kg/hr) is not known but was likely due to a dump stuck valve on the new EPGU or excessive water returns after the new EPGU was brought online. The geometric (geo) mean and arithmetic (ari) means of the 11 audits are presented and compared with those from the Rella et al. study that occurred in the Barnett Shale. Note that Audit 7th contributes to the significant increase in average emissions, however, the geometric means of the data sets are still comparable.

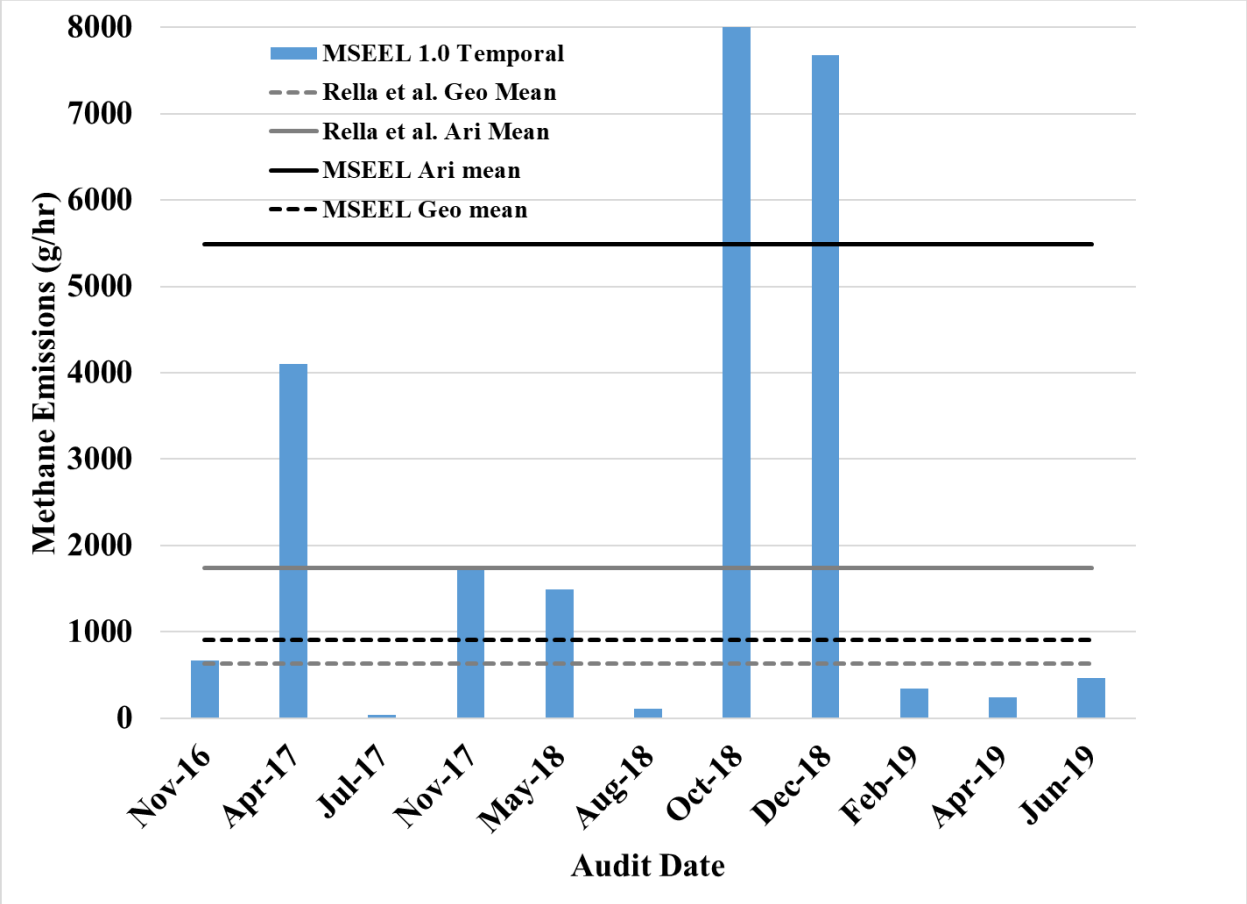

Figure 5.2: Update Temporal, Geometric, and Arithmetic Means for Methane Emissions from MSEEL 1.0 Audits.

Products

Oliver, Dakota. "Implications of Sampling Methods on Geospatial Mapping of Methane Sources," Master's Thesis, West Virginia University, 2019.

Plan for Next Quarter

- Complete 12th MSEEL 1.0 Audit
- Install OTM/Eddy-Covariance at MSEEL 1.0
- Review MSEEL 2.0 Activity to Modify Telemetry System
- Integrate Methane/Ethane 5 Hz UGGA into Full Flow Sampling System and Use in Audit 12

Topic 6 – Water Treatment

Approach

As part of this subtask, the Dr. Morrissey characterized the chemical and biological factors that influence radium accumulation in sludge from produced water.

This task is complete, and will not be updated in future quarters.

Results & Discussion

Milestone 1

- The concentrations of important scale forming cations (e.g. Ba and Sr) as well as Ra did not change over time during short term storage of produced water from well 3H.
- A relatively small amount of Ra precipitated from well 3H produced water during short term storage, 31.4 pg 226Ra/L on average (range 8.8 -76.6 pg 226Ra/L).
- Methane production averaged ~750 ugC/L during short term storage (20 days) and in general methane production was roughly one tenth the magnitude of carbon dioxide production

Milestone 2.

- Results from well 3H produced water suggests that one mole of sulfate precipitates ~0.8 moles of Ba. When Ba precipitates Ra concentrations decrease proportionally. In summary, SO4 causes Ra to accumulate in solid precipitate in proportion to its original concentration in the produced water sample via co-precipitation with Ba.
- Nutrient additions have no detectable impact on water chemistry dynamics in produced waters but increase CO2 production rates.

Topic 7 – Database Development

Approach

All MSEEL data is online and available to researchers (Figure 7.1 and 7.2). The website has been updated with the latest production beyond the end of the quarter (Figure 7.3). Work continues and we are adding data from MSEEL 3 Boggess Pad.

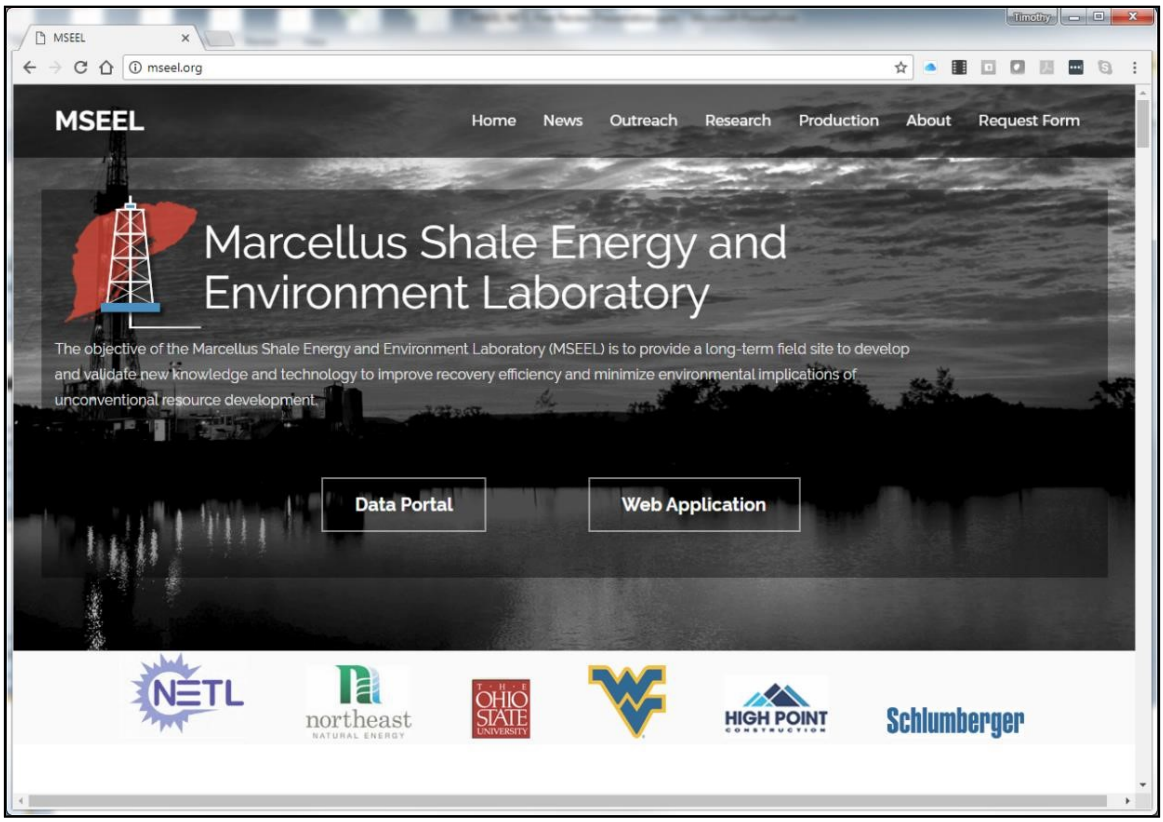

Figure 7.1: MSEEL website at **http://mseel.org/.**

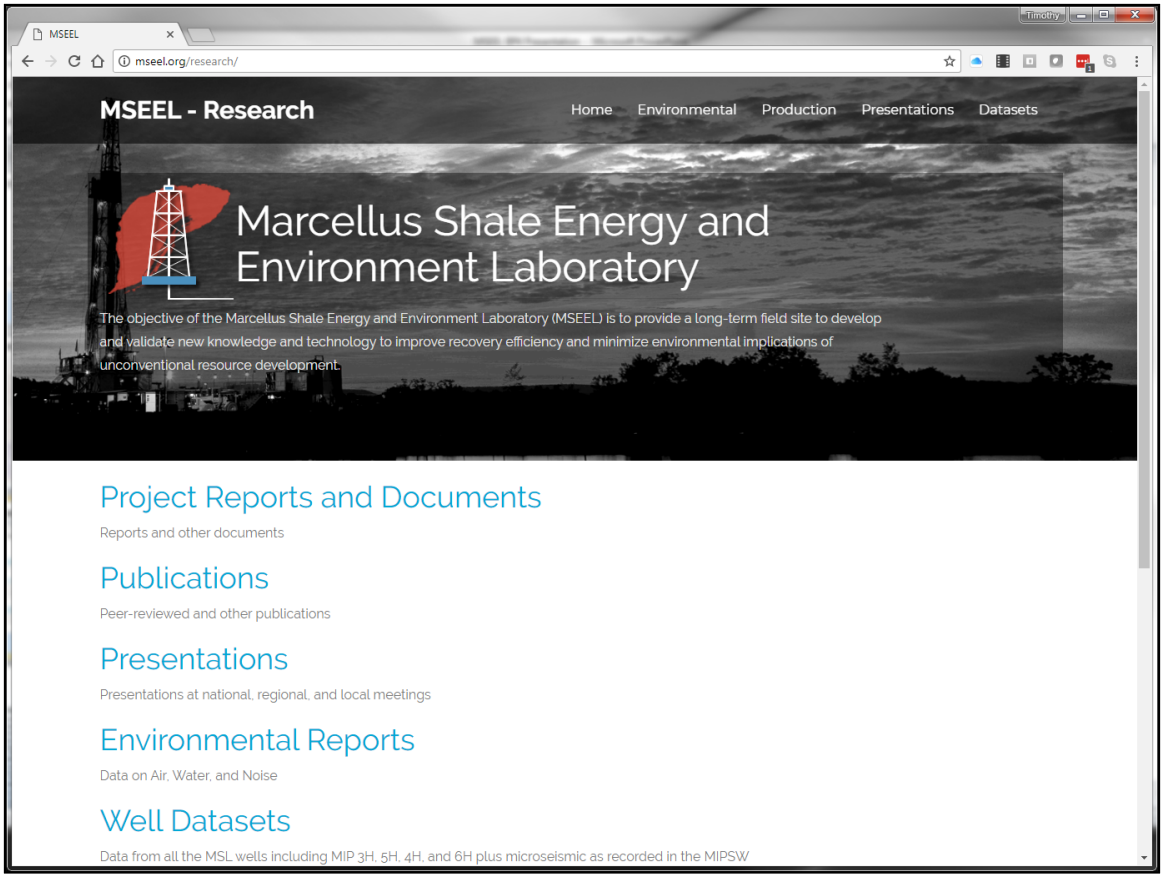

Figure 7.2: All data generated by the MSEEL project is available for download at **http://mseel.org/.**

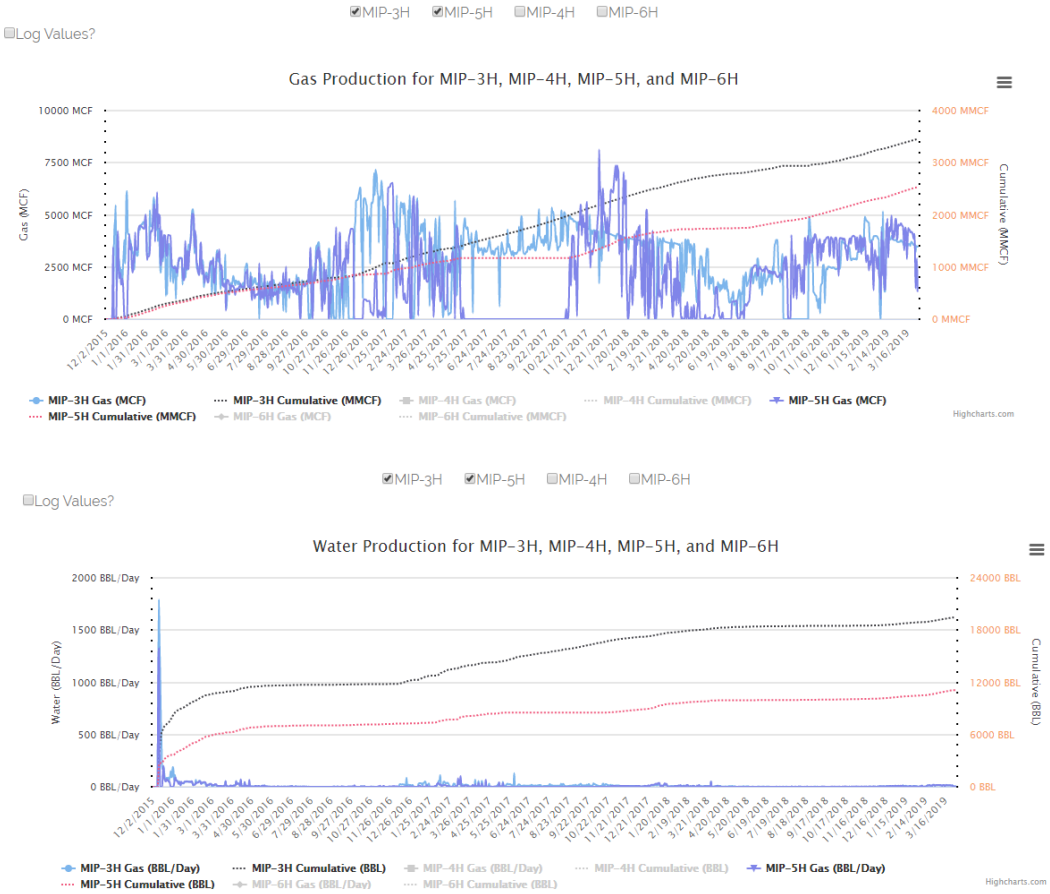

Figure 7.3: Gas and water production have been updated through the end of the quarter and are available at **http://mseel.org/**.

Results & Discussion

Data and publications are now available at http://mseel.org/.

Products

Web site enhanced and updated.

Plan for Next Quarter

Working to add data from the new Boggess Pad and improve data access.

Topic 8 – Economic and Societal

This task is complete and will not be updated in future reports.

Cost Status

Year 1

Start: 10/01/2014 End: 09/30/2019

Baseline Reporting Quarter

	Q1 (12/31/14)	Q2 (3/30/15)	Q3 (6/30/15)	Q4 (9/30/15)
Baseline Cost Plan	(From 424A, Sec. D)			
(from SF-424A)				
Federal Share	$549,000		$3,549,000	
Non-Federal Share	$0.00		$0.00	
Total Planned (Federal and Non-Federal)	$549,000		$3,549,000	
Cumulative Baseline Costs				
Actual Incurred Costs				
Federal Share	$0.00	$14,760.39	$237,451.36	$300,925.66
Non-Federal Share	$0.00	$0.00	$0.00	$0.00
Total Incurred Costs - Quarterly (Federal and Non-Federal)	$0.00	$14,760.39	$237,451.36	$300,925.66
Cumulative Incurred Costs	$0.00	$14,760.39	$252,211.75	$553,137.41
Uncosted				
Federal Share	$549,000	$534,239.61	$3,296,788.25	$2,995,862.59
Non-Federal Share	$0.00	$0.00	$2,814,930.00	$2,814,930.00
Total Uncosted - Quarterly (Federal and Non-Federal)	$549,000	$534,239.61	$6,111,718.25	$5,810,792.59

Start: 10/01/2014 End: 09/30/2019

Baseline Reporting Quarter

	Q5 (12/31/15)	Q6 (3/30/16)	Q7 (6/30/16)	Q8 (9/30/16)
Baseline Cost Plan	(From 424A, Sec. D)			
(from SF-424A)				
Federal Share	$6,247,367		$7,297,926	
Non-Federal Share	2,814,930		$4,342,480	
Total Planned (Federal and Non-Federal)	$9,062,297	$9,062,297.00	$11,640,406	
Cumulative Baseline Costs				
Actual Incurred Costs				
Federal Share	$577,065.91	$4,480,939.42	$845,967.23	$556,511.68
Non-Federal Share	$0.00	$2,189,863.30	$2,154,120.23	$0.00
Total Incurred Costs - Quarterly (Federal and Non-Federal)	$577,065.91	$6,670,802.72	$3,000,087.46	$556,551.68
Cumulative Incurred Costs	$1,130,203.32	$7,801,006.04	$10,637,732.23	$11,194,243.91
Uncosted				
Federal Share	$5,117,163.68	$636,224.26	$1,004,177.30	$447,665.62
Non-Federal Share	$2,814,930.00	$625,066.70	($1,503.53)	($1,503.53)
Total Uncosted - Quarterly (Federal and Non-Federal)	$2,418,796.68	$1,261,290.96	$1,002,673.77	$446,162.09

Start: 10/01/2014 End: 09/30/2019

Baseline Reporting Quarter	Q9 (12/31/16)	Q10 (3/30/17)	Q11 (6/30/17)	Q12 (9/30/17)
Baseline Cost Plan	(From 424A, Sec. D)			
(from SF-424A)				
Federal Share				$9,128,731
Non-Federal Share				$4,520,922
Total Planned (Federal and Non-Federal)				$13,649,653
Cumulative Baseline Costs				
Actual Incurred Costs				
Federal Share	$113,223.71	$196,266.36	$120,801.19	$1,147,988.73
Non-Federal Share	$0.00	$0.00	$0.00	$0.00
Total Incurred Costs - Quarterly (Federal and Non-Federal)	$113,223.71	$196,266.36	$120,801.19	$1,147,988.73
Cumulative Incurred Costs	$11,307,467.62	$11,503,733.98	$11,624535.17	$12,772,523.90
Uncosted				
Federal Share	$334,441.91	$138,175.55	$17,374.36	$700,190.63
Non-Federal Share	($1,503.53)	($1,503.53)	($1,503.53)	$176,938.47
Total Uncosted - Quarterly (Federal and Non-Federal)	$332,938.38	$136,672.02	$15,870.83	$877,129.10

Start: 10/01/2014 End: 09/30/2019

Baseline Reporting Quarter	Q13 (12/31/17)	Q14 (3/30/18)	Q15 (6/30/18)	Q15 (9/30/18)
Baseline Cost Plan	(From 424A, Sec. D)			
(from SF-424A)				
Federal Share				$11,794,054
Non-Federal Share				$5,222,242
Total Planned (Federal and Non-Federal)				$17,016,296.00
Cumulative Baseline Costs				
Actual Incurred Costs				
Federal Share	$112,075.89	$349,908.08	$182,207.84	$120,550.20
Non-Federal Share	$0.00	$31,500.23	$10,262.40	$4,338.00
Total Incurred Costs - Quarterly (Federal and Non-Federal)	$112,075.89	$381,408.31	$192,470.24	$124,888.20
Cumulative Incurred Costs	$12,884,599.79	$13,266,008.10	$13,458,478.34	$13,583,366.54
Uncosted				
Federal Share	$588,114.74	$238,206.66	$55,998.82	$2,600,771.62
Non-Federal Share	$176,938.47	$145,438.24	$135,175.84	$832,157.84
Total Uncosted - Quarterly (Federal and Non-Federal)	$765,053.21	$383,644.90	$191,174.66	$3,432,929.46

Start: 10/01/2014 End: 03/31/2019

Baseline Reporting Quarter	Q17 (12/31/18)	Q18 (3/31/19)	Q19 (6/30/19)	Q20 (9/30/19)
Baseline Cost Plan	(From 424A, Sec. D)			
(from SF-424A)				
Federal Share			$15,686,642.00	
Non-Federal Share			$9,037,442.00	
Total Planned (Federal and Non-Federal)			$24,724,084.00	
Cumulative Baseline Costs				
Actual Incurred Costs				
Federal Share	$80,800.03	$133,776.98	$714,427.48	
Non-Federal Share	$4,805.05	$130,449.21	$4,099,491.20	
Total Incurred Costs - Quarterly (Federal and Non-Federal)	$85,605.08	$264,226.19	$4,813,918.68	
Cumulative Incurred Costs	$13,668,971.62	$13,933,197.81	$18,747,116.49	
Uncosted				
Federal Share	$2,519,971.59	$2,386,194.61	$5,564,355.13	
Non-Federal Share	$827,352.79	$696,903.58	$412,612.38	
Total Uncosted - Quarterly (Federal and Non-Federal)	$3,347,324.38	$3,083,098.19	$5,976,967.51	

Appendix 1 – URTEC Submission #1

URTeC: 415

Marcellus Shale Energy and Environmental Laboratory (MSEEL) Results and Plans: Improved Subsurface Reservoir Characterization and Engineered Completions

Timothy R. Carr*[1], Payam Kavousi Ghahfarokhi[1], BJ Carney[2], Jay Hewitt[3], Robert Vagnetti[4]; 1. West Virginia University, 2. Northeast Natural Energy, 3 Hewitt Energy Strategies, 4. US Department of Energy, National Energy Technology Laboratory.

Copyright 2019, Unconventional Resources Technology Conference (URTeC) DOI 10.15530/urtec-2019-415

This paper was prepared for presentation at the Unconventional Resources Technology Conference held in Denver, Colorado, USA, 22-24 July 2019.

The URTeC Technical Program Committee accepted this presentation on the basis of information contained in an abstract submitted by the author(s). The contents of this paper have not been reviewed by URTeC and URTeC does not warrant the accuracy, reliability, or timeliness of any information herein. All information is the responsibility of, and, is subject to corrections by the author(s). Any person or entity that relies on any information obtained from this paper does so at their own risk. The information herein does not necessarily reflect any position of URTeC. Any reproduction, distribution, or storage of any part of this paper by anyone other than the author without the written consent of URTeC is prohibited.

Abstract

The Marcellus Shale Energy and Environment Laboratory (MSEEL) involves a multidisciplinary and multi-institutional team of universities companies and government research labs undertaking geologic and geomechanical evaluation, integrated completion and production monitoring, and testing completion approaches. MSEEL consists of two legacy horizontal production wells, two new logged and instrumented horizontal production wells, a cored vertical pilot bore-hole, a microseismic observation well, and surface geophysical and environmental monitoring stations. The extremely large and diverse (multiple terabyte) datasets required a custom software system for analysis and display of fiber-optic distributed acoustic sensing (DAS) and distributed temperature sensing (DTS) data that was subsequently integrated with microseismic data, core data and logs from the pilot holes and laterals. Comprehensive geomechanical and image log data integrated with the fiber-optic data across individual stages and clusters contributed to an improved understanding of the effect of stage spacing and cluster density practices across the heterogeneous unconventional reservoirs such as the Marcellus. The results significantly improved stimulation effectiveness and optimized recovery efficiency. The microseismic and fiber-optic data obtained during the hydraulic fracture simulations and subsequent DTS data acquired during production served as constraining parameters to evaluate stage and cluster efficiency on the MIP-3H and MIP-5H wells. Deformation effects related to preexisting fractures and small faults are a significant component to improve understanding of completion quality differences between stages and clusters. The distribution of this deformation and cross-flow between stages as shown by the DAS and DTS fiber-optic data during stimulation demonstrates the differences in completion efficiency among stages. The initial and evolving production efficiency over the last several years of various stages is illustrated through ongoing processing of continuous DTS. Reservoir simulation and history matching the well production data confirmed the subsurface production response to the hydraulic fractures. Engineered stages that incorporate the distribution of fracture swarms and geomechanical properties had better completion and more importantly production efficiencies. We are working to improve the modeling to understand movement within individual fracture swarms and history match at the individual

stage. As part of an additional MSEEL well pad underway incorporates advanced and cost-effective technology that can provide the necessary data to improve engineering of stage and cluster design, pumping treatments and optimum spacing between laterals, and imaging of the stimulated reservoir volume in the Marcellus and other shale reservoirs.

Introduction

The multidisciplinary and multi-institutional MSEEL team worked on geoscience, engineering, and environmental research in collaboration with Northeast Natural Energy LLC., several industrial partners, and the National Energy Technology Laboratory of the US Department of Energy. The objective of the Marcellus Shale Energy and Environment Laboratory (MSEEL) is to provide a long-term collaborative field site to develop and validate new knowledge and technology to improve recovery efficiency and minimize environmental implications of unconventional resource development. MSEEL began on the fall of 2015 with the drilling across from the City of Morgantown, West Virginia of the Northeast Natural Energy MIP-3H and MIP-5H and the vertical MIP-SW scientific and microseismic observation well. The site incorporates data from MIP-4H and MIP-6H wells, previously drilled in 2011. Logs were run on the lateral of the MIP-3H, and the MIP-3H was instrumented with a permanent fiber-optic cable (Figure 1). A cored vertical pilot bore-hole, a microseismic observation well, and surface geophysical and environmental monitoring stations completed the site. We have reported on numerous environmental observations, which show that the drilling, completion and production of the wells has had minimal environmental impact (e.g., Hakala et al. 2017; Sharma et al. 2017; Ziemkiewicz, 2017). The MIP production wells at the MSEEL site can easily supply the entire gas demand of the city. This paper will concentrate on the comprehensive geomechanical and image log data on the MIP-3H and integration with the fiber-optic data across individual stages and clusters. The results contributed to an improved understanding of the effect of stage spacing and cluster density practices across the heterogeneous unconventional shale reservoirs such as the Marcellus, and significantly improved stimulation effectiveness and optimized recovery efficiency.

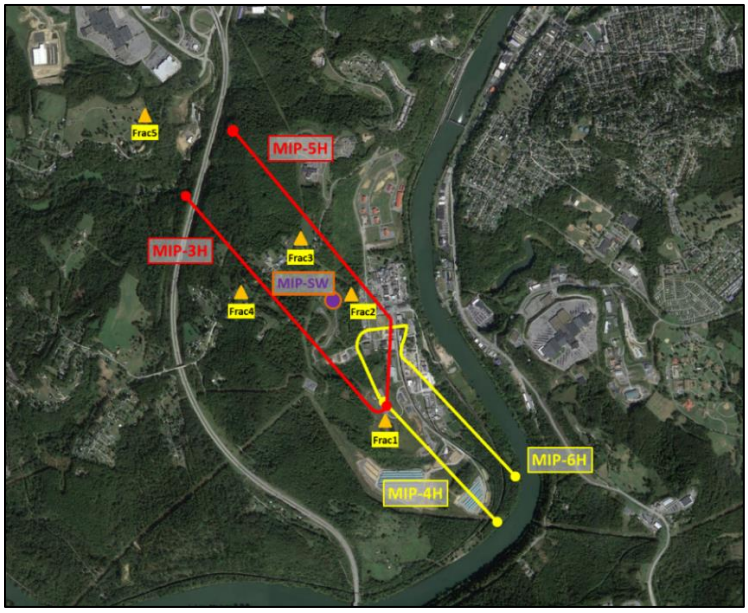

Figure 1. The Marcellus Shale Energy and Environment Laboratory (MSEE) is located across the Monongalia River from Morgantown, West Virginia. The MSEEL site consists of four horizontal production wells (MIP), one scientific/microseismic observation well (purple dot), and five surface seismic stations (yellow triangles).

Methods/Procedures

As part of the MSEEL project two new horizontal wells MIP-3H and MIP-5H were completed in 2015. Fiber optics technology including distributed acoustic sensing (DAS) and distributed temperature sensing (DTS) were deployed in the MIP-3H horizontal well to provide continuous subsurface vibration and temperature sampling during stimulation. The entire lateral of the MIP-3H was logged with a comprehensive suite of logs including geomechanical and image logs. The MIP-3H stimulation over 28 stages involved injection, at high pressure, averaging 8500 psi (58.6 MPa), to break the formation and establish a complex network of permeable fracture pathways. Microseismic data was recorded at the MIP-SW well located between the MIP-3H and MIP-5H (Figure 1). Microseismic events were numerous and displayed a consistent N59^{o}E orientation (Figure 2) (Wilson et al. 2018). The microseismic events showed wide vertical variation between stages with most events located in the units well above the landing zone in the lower Marcellus Shale (Figure 2). Logging of the MIP-3H lateral indicated several small faults and more than 1,600 fractures healed with calcite cement (Carr et al. 2017). Most fractures observed in the lateral were oriented N85^{o}E. Natural fractures provide planes of weakness that can play a significant role in production performance of shale wells by capturing induced fractures during stimulation and contributing to a complex fracture network during hydraulic fracturing.

The extremely large and diverse (multiple terabyte) datasets required a custom software system for analysis and display of fiber-optic DAS and DTS data and subsequent integration with microseismic data, core data and logs from the pilot holes and laterals. As an example, stage 10 contained over 150 fractures and several faults. Comprehensive geomechanical and image log data integrated with the fiber-optic data across individual stages and clusters contributed to an improved understanding of the effect of stage spacing and cluster density practices across the heterogeneous unconventional reservoirs such as the Marcellus.

Results

Among other attributes, temperature, energy and instantaneous frequency were calculated for several stimulated stages in MIP-3H lateral. One common way to visualize the DTS and DAS data is to use a waterfall plot with the measured depth of the well on the vertical axis and number of the timesteps in the horizontal axis. The color shows the calculated temperature or energy attribute for that timestep. The MIP-3H stimulation over 28 stages involved injection, at high pressure, averaging 8500 psi (58.6 MPa), to break the formation and establish a complex network of permeable fracture pathways Stage 10 shows the stimulation (Figure 3c), and the expected cooling of stage 10 as large quantities of surface-temperature water are injected into the reservoir with a temperature approaching 170^{o}F. The plug-and-perf mechanism is employed for the completion of the MIP-3H. This procedure seals the direct connection between Stage 10 and Stage 9 through the wellbore, and leakage around the plug or through cemented annulus as cooling in the previous Stage 9 was not observed (Figure 3a). Stage 10 DAS amplitude shows and uneven stimulation with energy concentrated in clusters 1, 2 and 5 (Figure 3b). The energy plot does not reveal detectable energy for Stage 9 (Figure 3b). However, expanding the scale of the DTS waterfall plot to encompass warming shows warming of Stage 9 during stimulation of Stage 10 (Figure 4a). Amini et al., 2017 and Carr et al., 2017 noticed this temperature rise for several other stages in MIP-3H. They suggested that numerous fractures and fault close to the stage boundaries are possibly responsible for this abnormal observation. Ghahfarokhi et al., 2019 showed evidence for long-period long-duration seismic events resulted from fault and fractures re-activation. Stimulation of the Stage 9 took place around 2 hours before Stage 10 stimulation. The fracturing fluid of Stage 9 rested at the formation and got warmed and approached reservoir temperature. Subsequent stimulation of Stage 10 pushed the warmed fluid of stage 9 back toward the well through fractures and faults. High fracture intensity close to the base of the Stage 10 and top of the Stage 9 were observed in wireline image logs (Carr et al. 2017).

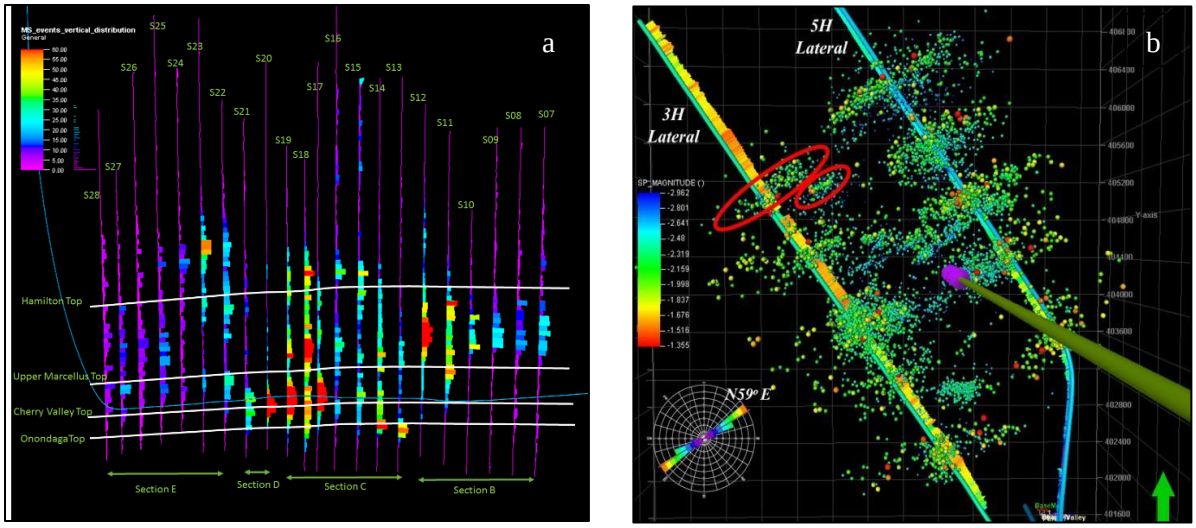

Figure 2. (a) The vertical distribution of microseismic events varies significantly along the MIP-3H lateral and is concentrated significantly above the landing zone in the lower Marcellus Shale. (b) The orientation of microseismic events in both the MIP-3H and MIP-5H is consistently N59°E and like other wells in north-central West Virginia and southwest Pennsylvania. Image (b) modified from Wilson et al., 2018.

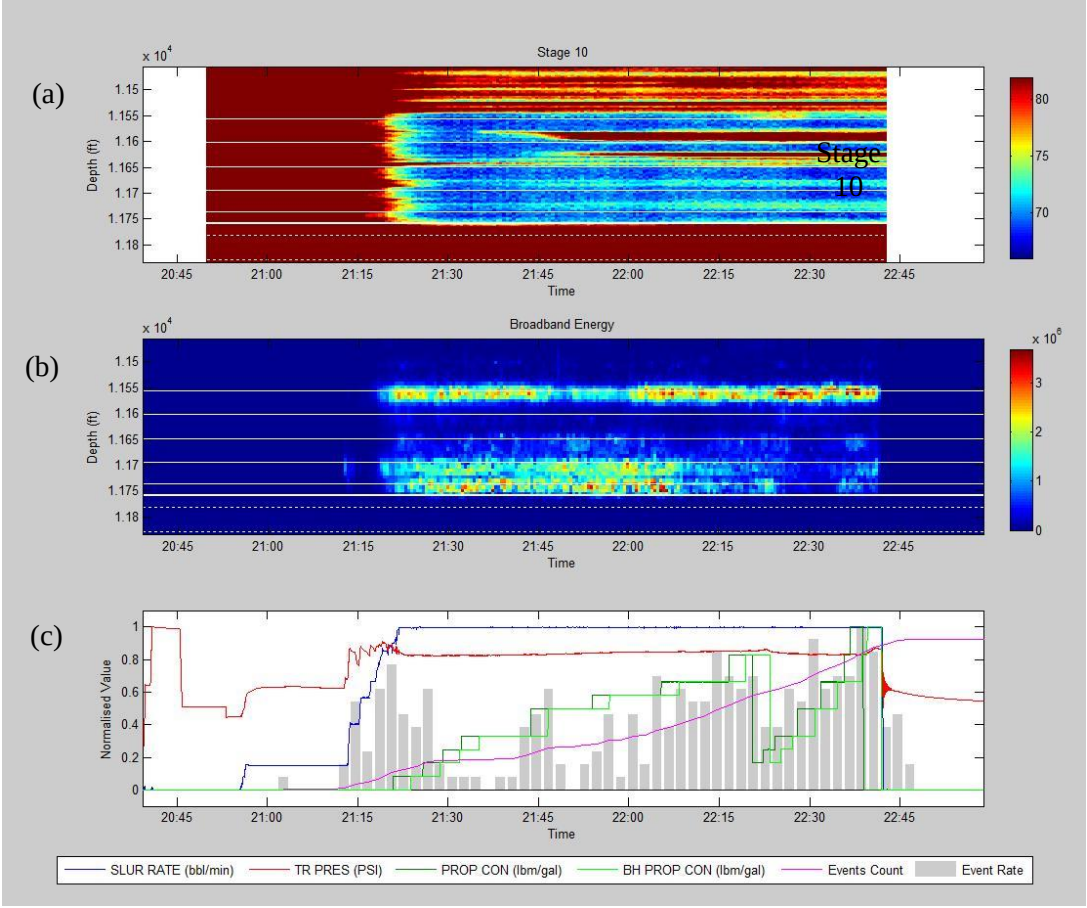

Figure 3. (a) Waterfall plot of distributed temperature sensing (DTS) data for Stage 10 and part of the previous Stage 9 and a portion of the lateral toward the heel showing the significant cooling of Stage 10 as large quantities of fracture fluid and proppant at near surface temperature are injected in the Marcellus Shale reservoir. (b) Waterfall plot of distributed acoustic sensing data (DAS) as broadband energy for Stage 10 and part of the previous Stage 9 showing the uneven distribution with energy concentrated in clusters 1, 2 and 5. Clusters 3 and 4 appear to be unstimulated. (c) Pumping scheduled for Stage 10 plotted on the same time scale as the DTS and DAS waterfall plots. Image modified from Kavousi Ghahfarokhi et al., 2018.

Kavousi Ghahfarokhi and others (2018) applied several common seismic attributes to the DAS data. These attributes in addition to energy include instantaneous attributes, and dominant frequency. The computations were undertaken through custom processing software developed in the MSEEL research group at West Virginia University. Low frequency zone identified in instantaneous frequency attribute was observed in Stage 9 (Figure 4b). This was attributed to presence of fluid that transferred cross-stage during hydraulic fracturing, and the frequency damping of the vibrations around the fiber (Kavousi Ghahfarokhi et al., 2018).

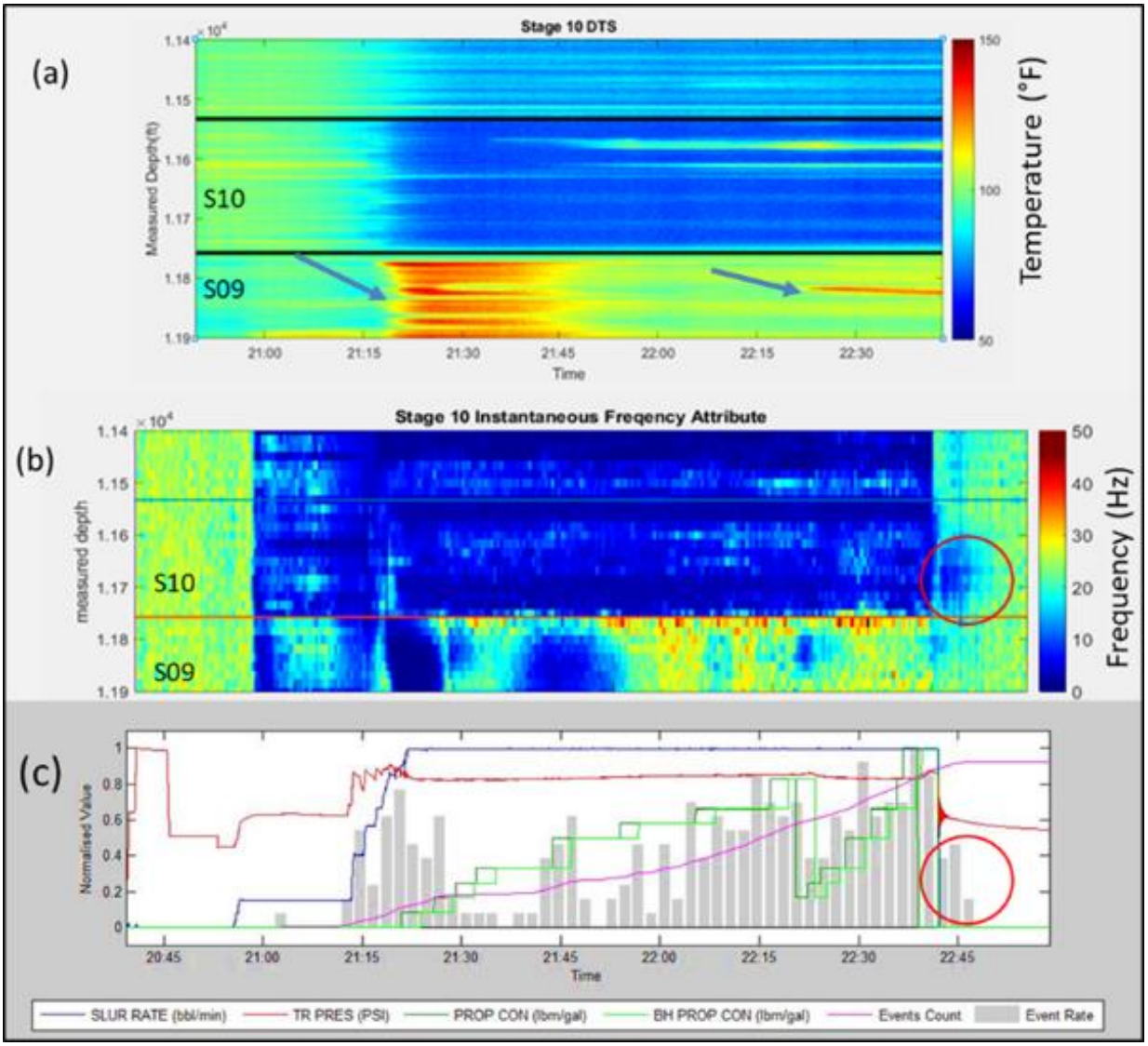

Figure 4. (a) Waterfall plot of distributed temperature sensing (DTS) data for Stage 10 and part of the previous Stage 9 and a portion of the lateral toward the heel showing the significant cooling of Stage 10 as large quantities of fracture fluid and proppant at near surface temperature are injected in the Marcellus Shale reservoir. Scale has been expanded from Figure 3a. Note warming observed in Stage 9 during stimulation of Stage 10. (b) Plot of instantaneous frequency. Low frequency zones are observed when there is a temperature rise in Stage 9. Note that the decreased injection of proppant also creates low frequency zones in Stage 9. Clusters 3 and 4 appear to be unstimulated. (c) Pumping scheduled for Stage 10 plotted on the same time scale as the DTS and DAS waterfall plots. Image modified from Kavousi Ghahfarokhi et al., 2018.

Discussion

A conceptual model was proposed as an attempt to explain the effect of the numerous preexisting N85°E healed fractures and faults observed in logs with observations during fracture stimulation in the MIP-3H (Figure 5). These observations during fracture stimulation include: clusters of microseismic events centered well above the lateral and orientated N59°E, and the observed significant warming as measured by DTS and attributes as computed from DAS such as instantaneous frequency in previous stages associated with fractures in the lateral. The rapid injection during fracture stimulation of an average of 255 cubic feet of proppant and fluid for every foot of the 6,058 feet (1846m) completed lateral would rapidly change both pore pressure, and vertical and lateral stresses. With the N36°W orientation of the MIP-3H lateral (Figure 1), fracturing and injection could occur along non-critically oriented N79°E preexisting fractures in the lower Marcellus Shale and predominately expessed in the aseismic "slow slip" with low frequency seismic events that are not picked up by standard microseismic monitoring. Such low frequency events have been observed in surface seismometers, downhole geophones and DAS data during stimulation of Stage 10 (Ghahfarokhi et al., 2019). The oblique orientation of the lateral to prexisting fractures could explain the warming as detected by DTS of previous stages to near formation temperatures by movement of fluids previously injected and warmed by the formation through stimulated fractures communicating from one stage to the previous stage(s). This change in temperature in the previous stage(s) appears to be more prevalent between stages with numerous observed faults and fractures. Microseismic events are centered significantly above the stimulated interval and follow optimal oriented fractures to the present day stress regime. The observed microseismic events may not be a direct expression of stimulated fractures and propopant placement in the targeted lower Marcellus shale, but indirect expression in the overlying stratigraphic units imposed by the injection of more than 250 cubic feet of sand and fluid per foot of lateral.

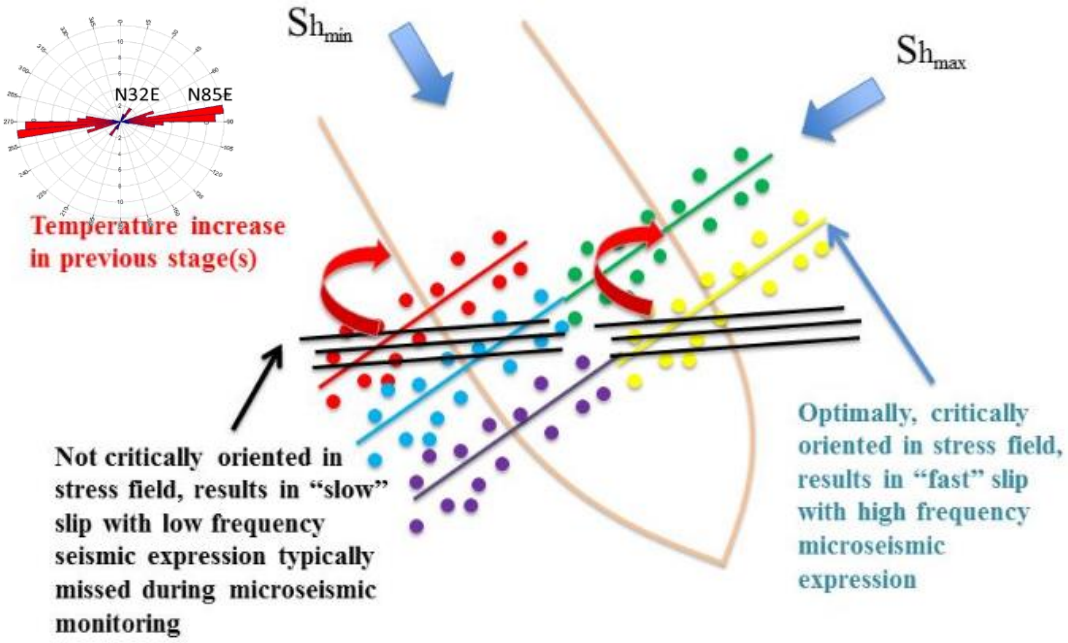

Figure 5. Conceptual model of observed pattern of the numerous preexisting N85°E fractures and faults observed in logs and plotted on the Rose diagram, microseismic orientated N59°E, warming observed in DTS in previous stages during fracture stimulation in the MIP-3H. Basic figure was modified from Das and Zoback, 2012. Movement and injection along non-critically oriented preexisting fractures in the lower Marcellus Shale resulted in the "slow" slip with low frequency seismic expression that was not picked up by microseismic monitoring and movement of fluids warmed by the formation to previous stimulated stages. Microseismic events follow optimal oriented fractures to the present-day stress regime and are centered significantly above the stimulated interval. The observed microseismic events may be the expression of the stress on overlying layers imposed by the injection of more than 250 cubic feet of sand and fluid per foot of lateral.

Stages 13 through 19 were designed using geomechanical properties from the logs along the lateral. Comparing the geomechanical moduli and properties between the geometric stage 10 and one of the engineered stages such as Stage 14 shows the wide scatter of geomechanical moduli and properties in stage 10 and the tighter cluster in Stage 14 (Figure 6). Stage 14 shows a more even fracture stimulation. DTS dated collected since early 2016 to the present and processed with MSEEL software illustrates temperature variations for each stage relative to daily average temperature of each stage along the well (Figure 7) (Carr et al. 2018). On the production de-trended DTS attribute, general cooling from the heel to the toe is observable, but some geometric stages such as 10 and 11 and 20-21 and 23-28 are relatively warmer. Also standing out are the cooler engineered stages 17-19. Based on the processed DTS data, the non-optimum stimulation of Stage 10 appears to have resulted in apparent non-optimum production (Carr et al. 2007; Amini et al. 2007 and Ghahfarokhi et al. 2018). Using production logs and DTS data production in engineered stages 13 through 19 appear to have on average increased production 20 percent compared to the geometric completion techniques (Figure 8).

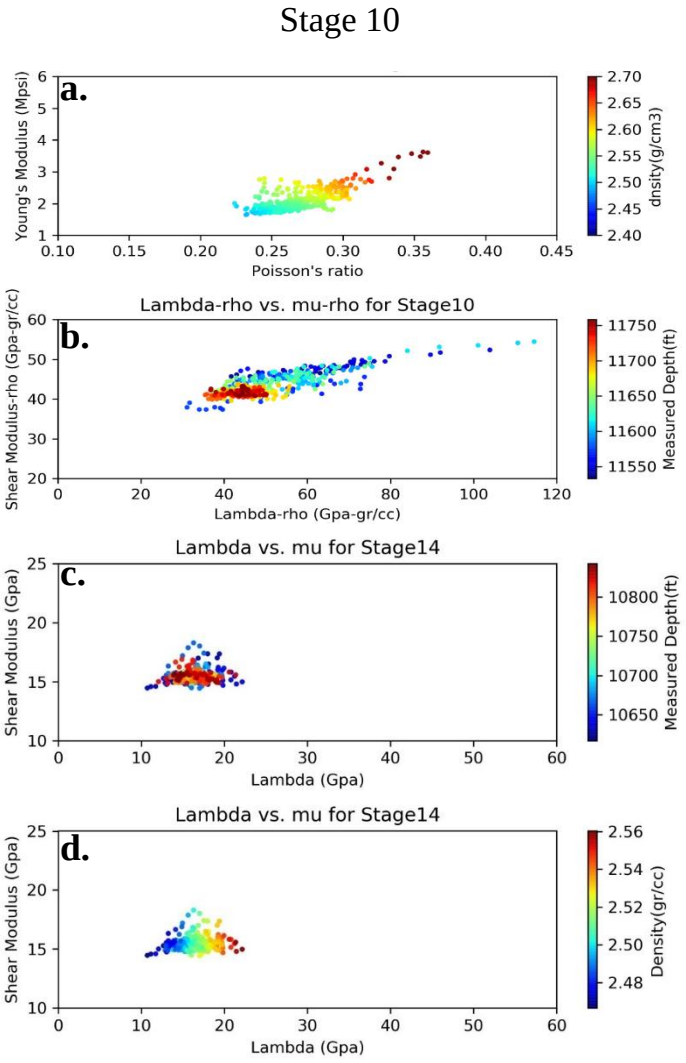

Figure 6. (a) Poisson's Ratio versus Young's Modulus for geometric Stage 10 attributed with density showing the scatter. Density for higher values approach calcite (2.71 gm/cc). (b) Lambda-rho versus mu-rho plot for geometric Stage 10 attributed with depth along the stage. (c) Lambda versus mu for engineered Stage 14 attributed with depth along the stage. (d) Lambda versus mu for engineered Stage 14 attributed with density along the stage. The engineered Stage 14 shows a tighter distribution of geomechanical properties, which is believed to have resulted in higher stimulation efficiency than geometric Stage 10.

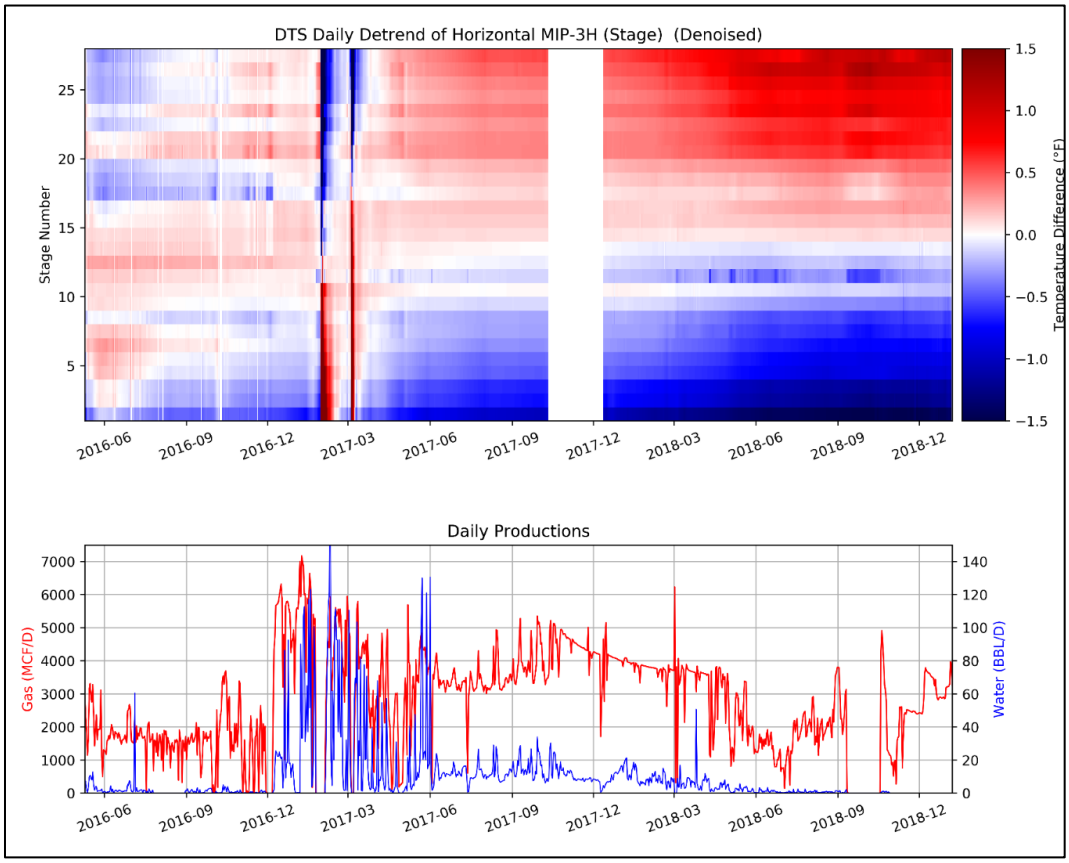

Figure 7. The de-trended DTS attribute is averaged to the stage scale. The vertical lines show the time that MIP-3H was cleaned out with water and then with nitrogen foam prior to production logging. Geometric Stage 10 shows a higher temperature that is attributed to lower gas production. Modified and updated from Carr et al. 2018.

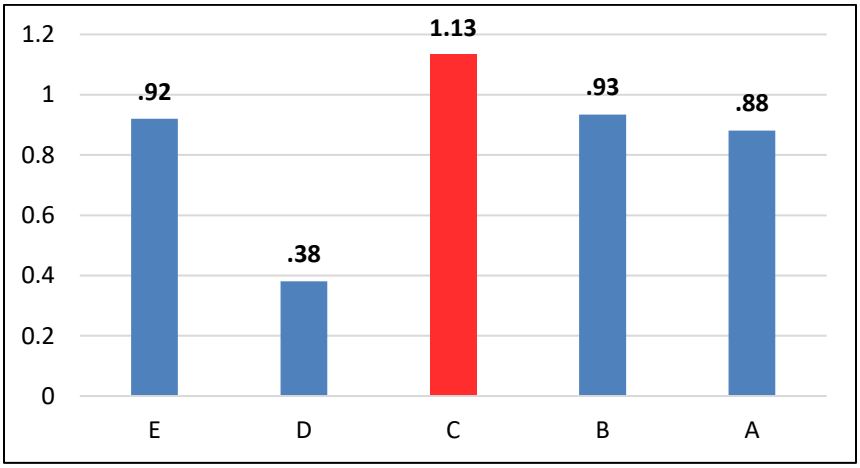

Figure 8. MIP 3H gas production (mcf/ft) showing that the engineered design for stages 13 through 19 represented by C using data obtained during production logging of the MIP-3H. Engineered stages in section C have approximately 20% increased production compared to standard geometric completion techniques. EUR for future wells could be 10-20% greater if one can exploit the technologic advantages gained through MSEEL in a more cost-effective fashion

Conclusions

An improved understanding of stimulation efficiency is obtained from integration of the extremely large and diverse (multiple terabyte) datasets using a custom software system for analysis and display of fiber-optic distributed acoustic sensing (DAS) and distributed temperature sensing (DTS) data integrated with completion observation, microseismic data, core data and logs from the pilot holes and laterals. Comprehensive geomechanical and image log data along with processed DAS and DTS data across individual stages and clusters contributed to an improved understanding of the effect of stage spacing and cluster density practices across the heterogeneous unconventional reservoirs such as the Marcellus Shale. The results significantly improved stimulation effectiveness and appears to have improved recovery efficiency.

Microseismic and fiber-optic data obtained during the hydraulic fracture simulations and subsequent DTS data acquired during production serves as constraining parameters to evaluate stage and cluster efficiency on the MIP-3H well. Deformation effects and complexity related to preexisting fractures and small faults are a significant component of completion quality differences between stages and clusters. DAS and DTS fiber-optic show the effect of this deformation and cross-flow between stages during stimulation and demonstrates the differences in completion efficiency among stages.

Ongoing processing of continuous DTS illustrates initial and evolving production efficiency over the last several years of various stages. Reservoir simulation and history matching the well production data confirmed the subsurface production response to the hydraulic fractures. Engineered stages that incorporate the distribution of fracture swarms and geomechanical properties had better completion and more importantly production efficiencies. We are working to improve the modeling to understand movement within individual fracture swarms and history match at the individual stage.

As part of ongoing work with DTS and DAS monitoring at the MIP-3H and an additional MSEEL well pad underway we will incorporate next-generation cost-effective technology to determine feasibility of applying lessons learned on an "every well" basis to improve engineering of stage and cluster design, pumping treatments and optimum spacing between laterals, and imaging of the stimulated reservoir volume in the Marcellus and other shale reservoirs. MSEEL is working to evaluate and leverage this improved understanding gained to drill better wells by increasing gas recovery while minimizing wellbore risk and lower costs.

References

Carr, T.R., Wilson, T.H., Kavousi, P., Amini, S., Sharma, S., Hewitt, J., Costello, I., Carney, B.J., Jordon, E., Yates, M. and MacPhail, K. 2017. Insights from the Marcellus Shale Energy and Environment Laboratory (MSEEL). Unconventional Resources Technology Conference held in Austin, Texas, USA, 24-26 July 2017. 9p., https://doi.org/10.15530/URTEC-2017-2670437.

Carr, T. R., Kavousi Ghahfarokhi, P. Carney, BJ., Hewitt, J., and Vagnetti, R. 2018. A New Algorithm for Processing Distributed Temperature Sensing (DTS), Conference Proceedings Eastern Section Society Petroleum Engineers, Society Petroleum Engineers, 7-11 October, Pittsburgh, PA, SPE-194814-18ERM-MS, 16p. https://doi.org/10.2118/191814-18ERM-MS .

Hakala, J.A.; Crandall, D.; Moore, J.; Phan, T.; Sharma, S.; Lopano, C. Laboratory-scale studies on chemical reactions between fracturing fluid and shale core from the Marcellus Shale Energy and Environmental Laboratory (MSEEL) site. Unconventional Resources Technology Conference, Austin, TX, 24 – 26 July, https://doi.org/10.15530-urtec-2017-2670856.

Kavousi, P., Carr, T., Wilson, T., Amini, S., Wilson, C., Thomas, M., MacPhail, K., Crandall, D., Carney, B.J., Costello, I. and Hewitt, J. 2017. Correlating distributed acoustic sensing (DAS) to natural fracture intensity for the Marcellus Shale. In *SEG Technical Program Expanded Abstracts 2017* (pp. 5386-5390). Society of Exploration Geophysicists. https://doi.org/10.1190/segam2017-17675576.1

Kavousi Ghahfarokhi, P., Carr, T., Song, L., Shukla, P. and Piyush P. 2018. Seismic Attribute Application for the Distributed Acoustic Sensing Data for the Marcellus Shale: A New Insights to Cross-Stage Flow Communication. SPE Hydraulic Fracturing Technology Conference held in The Woodlands, TX, USA, 23-25 January 2018. https://doi.org/10.2117/189888-MS.

Kavousi Ghahfarokhi, P., Wilson, T.H., Carr, T.R., Kumar, A., Hammack, R. and Di, H., 2019. Integrating distributed acoustic sensing, borehole 3C geophone array, and surface seismic array data to identify long-period long-duration seismic events during stimulation of a Marcellus Shale gas reservoir. Interpretation, *7*(1), pp. SA1-SA10. https://doi.org/10.1190/INT-2018-0078.1.

Sharma S., Carr, T. R., Mouser, P. J., Wrighton, K., Cole, D., Wilkins, M., Darrah, T., and Hakala, A. 2017. Biogeochemical Characterization of Core, Fluids, and Gas at MSEEL Site. Unconventional Resources Technology Conference held in Austin, Texas, USA, 24-26 July 2017. 8p. https://doi.org/10.15530/urtec-2017-2669965.

Wilson, T. H., Carr, T., Carney, BJ., Yates, M., MacPhail, K., Morales, A., Costello, I., Hewitt, J., Jordon, E., Uschner, N., Thomas, M., Akin, S., Oluwaseun, M., Asbjoern J., Hogarth, L., Anifowoshe, O., and Naseem, K. 2018. Marcellus Shale model stimulation tests and microseismic response yield insights into mechanical properties and the reservoir DFN. Interpretation, 6(2), T231-T243. Volume 6, Issue 2 (May 2018), Society Exploration Geophysicists. https://doi.org/10.1190/int-2016-0199.1.

Ziemkiewicz, P.F. 2017. The Marcellus Shale Energy and Environmental Laboratory (MSEEL): Water and Solid Waste Findings--Year One. Unconventional Resources Technology Conference held in Austin, Texas, USA, 24-26 July 2017. 9p. https://doi.org/10.15530/urtec-2017-2669914.

Appendix 2 – URTEC Submission #2

URTeC: 650

Fracture analysis before and after Hydraulic Fracturing in the Marcellus Shale using the Mohr-Coulomb failure criteria

Kaitlin Evans[1], Randy Toth[1], Tobi Ore[1], Jarrett Smith[1], Natalia Bannikova[1]
Timothy Carr[1], Payam Kavousi Ghahfarokhi[1]
[1]Department of Geology and Geography, West Virginia University, Morgantown, WV

Copyright 2019, Unconventional Resources Technology Conference (URTeC) DOI 10.15530/urtec-2019-650

This paper was prepared for presentation at the Unconventional Resources Technology Conference held in Denver, Colorado, USA, 22-24 July 2019.

The URTeC Technical Program Committee accepted this presentation on the basis of information contained in an abstract submitted by the author(s). The contents of this paper have not been reviewed by URTeC and URTeC does not warrant the accuracy, reliability, or timeliness of any information herein. All information is the responsibility of, and, is subject to corrections by the author(s). Any person or entity that relies on any information obtained from this paper does so at their own risk. The information herein does not necessarily reflect any position of URTeC. Any reproduction, distribution, or storage of any part of this paper by anyone other than the author without the written consent of URTeC is prohibited.

Abstract

Data obtained from the Marcellus Shale Energy and Environment Laboratory (MSEEL) project was used to understand how pre-existing fractures behave under elevated pore pressure. 1680 pre-existing fractures were identified along the lateral of the MIP-3H well. Image logs and 3D computer tomography (CT) scan of the cores was used for fracture location and most fractures were identified as calcite-filled and resistive. In addition, sonic scanner well logs provided minimum horizontal stresses for every few feet, and the pilot-hole density log provided the vertical stress at each point along the lateral. This collection of geologic and geomechanical data helped us to establish an anisotropic stress field with separate stress tensors for each stage. Twenty-eight stress tensors were constructed corresponding to twenty-eight completion stages within the MIP-3H well. The vertical stress component of the tensors was calculated by integrating MIP-3 pilot-hole density log to the average depth of each stage. The minimum horizontal stresses (Shmin) were also calculated by averaging the recorded Shmin readings in each stage. Maximum horizontal stress (Shmax) was calculated by a third-party logging vendor by adding a 400 psi to the Shmin values. The stress tensors were transformed into a geographic coordinate system along with the dip and strike of each fracture. The transformed coordinate system (North-East-Down) was used when applying Cauchy's Stress theorem to every singular fracture within each stage to calculate the normal and shear stress components on each fracture. A Mohr diagram was created for each stage with two failure criteria lines corresponding to mu (μ) values of 0.6 and 1.0. Fractures are displayed on the diagram using their calculated normal and shear stresses. The pore pressure increase found from the average treatment pressure for each stage was applied and whether natural fractures experienced tensile or shear failure was inspected. The objective is to understand if natural fractures experience shear failure or tensile failure during hydraulic fracturing and determine if there is a contrast in the response between resistive (calcite-filled) and conductive

fractures. It was observed that prior to hydraulic fracturing, resistive natural fractures are mechanically dead and are in the stable region of the Mohr diagrams. Results show that although the majority of the pre-existing fractures are identified as resistive and mineral-filled, they undergo tensile failure when pore pressure was increased during hydraulic fracturing.

Introduction

Unconventional oil and gas plays have become major producers globally and have transformed the United States energy sector. Unconventional shale wells have resulted in abundant natural gas energy for the U.S., and research by corporations such as MSEEL are working toward efficient hydraulic fracturing while minimally impacting the environment. The Marcellus Shale is one of the largest unconventional plays in the world and extends throughout much of the Appalachian basin (Figure 1a) (Wang and Carr, 2013). Because shale reservoirs have very little permeability, induced permeability is required to allow for hydrocarbon flow. Creating permeability within the source rock is one main concern when hydro-fracturing a mudstone formation. Carr et al. (2017) suggests that understanding the distribution and influence of these pre-existing fractures is vital when improving completions in a well. The idea that the majority of reservoir stimulation is through the reactivation of pre-existing fractures rather than the creation of new fractures is generally accepted and that those pre-existing fractures affect the stimulation process. It is essential that these fractures open when hydraulically stimulated because pre-existing fractures contribute considerably more to the creation of permeable pathways by fracture network than those induced during the fracture process. The reactivation of these pre-existing fractures is key to successful unconventional well production.

With sufficient data, it is possible to plot the fractures as points on a three-dimensional Mohr diagram (Zoback, 2010). The orientation of the maximum horizontal stress in this area was determined to be N57°E by analysis of microseismic trends. (Wilson and Sullivan, 2016; Wilson et al., 2018). Shmin was assumed to be in the direction 90° off of Shmax. The largest principal stress was found to be the vertical stress (Sv) and the state of the stress as normal faulting. The direction of the stresses was then used to create a tensor transformation in order to eliminate the shear stresses (Zoback, 2010). Using this information, the fractures were plotted on a Mohr diagram to observe the change in stress state.

Background

The data used in this work came from the Marcellus Shale Energy and Environmental Laboratory (MSEEL) project. MSEEL consists of a multidisciplinary and multi-institutional team in engineering, geosciences and environmental research (Carr et al., 2017). The purpose of this research is to identify the best practices for optimizing hydraulic fracture stimulation while minimizing environmental impacts of unconventional resource development (Carr et al., 2017). Multiple wells have been drilled and completed for the MSEEL project, but the focus of this research is on data collected from the MIP-3H well.

Viable production of unconventional, shale-gas reservoirs requires hydraulic stimulation of multiple stages. Completion of this well included stimulation of 28 stages within five sections: A, B, C, D, and E. Stimulation of the reservoir stage to stage included high pressure injection

averaging 8500 psi. The length of each stage was around 200 feet with four to five clusters per stage.

The MIP-3H well was drilled with N36°W heading within a section of the Marcellus roughly 100m thick. The MIP-3H was drilled just above the Cherry Valley Limestone at the transition between the upper and lower section of the formation and targets the high gamma-ray and organic-rich zone (Wilson et al., 2018).

During the Acadian Orogeny, large volumes of deltaic sediments were deposited within the Acadian Foreland Basin. This delta complex is comprised of two primary delta systems: 1) The Catskill Delta of Middle to Late Devonian age and 2) The Price-Rockwell Delta of Late Devonian to Early Mississippian age (Lash et al., 2011). The foreland basin-delta complex sedimentary wedges are responsible for the high volume of sediment influx into the Appalachian Basin (Lash et al., 2011). Relief caused by uplifting episodes acted as the sediment source feeding the delta systems. Clastic particles comprising the Marcellus Shale were sourced from the Catskill Delta (Lash et al., 2011). Rapid subsidence in the region resulted in a transgressional sequence that ultimately deposited the black shales of the Marcellus. These black shales were formed in the relatively deep, anoxic bottom water conditions of the epeiric sea parallel to the mountain chain (Chen et al., 2017). Radiometric age dating of the Marcellus Shale places the formation in the Middle Devonian at approximately 384 Ma (Chen et al., 2017).

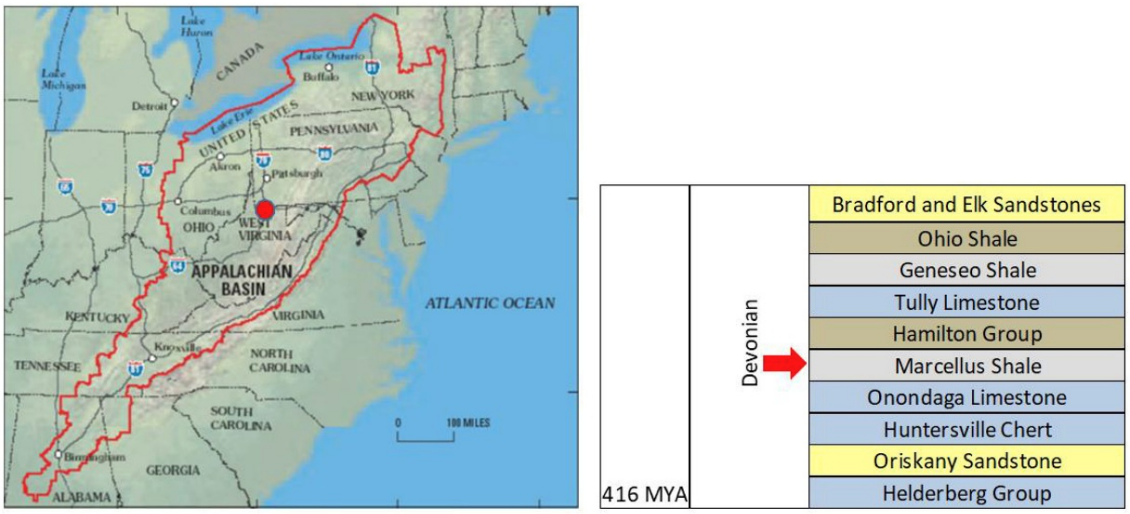

Figure 1 extent of the Appalachian Basin and the location of the MIP-3H well (a) along with the stratigraphic position of the Marcellus (b) adapted from (Bhattacharya, et al. 2019).

Two major natural fracture sets, J1 and J2, have been identified within the Marcellus (Engelder and Lash, 2009). Folding of the J1 set and bedding planes show that the J1 set formed early and most likely in response to high fluid pressure from the thermal maturation of organic material

(Engelder and Lash, 2009). The J2 joint set may have formed in response to the formation of the fold and thrust belts that make up the Appalachian Valley and Ridge province (Engelder and Lash, 2009). Several subsurface studies have been completed in the area showing a N80°E set of fractures that corresponds with the J1 set and a N64°W set with an orientation similar to the J2 set (Engelder and Lash, 2009; Evans, 1980; Wilson et al., 2018).

Methodology

Azimuth values of pre-existing fractures within each stage were recorded using wireline image logs, as well as the P32 fracture intensity. This is the fracture area per unit volume.

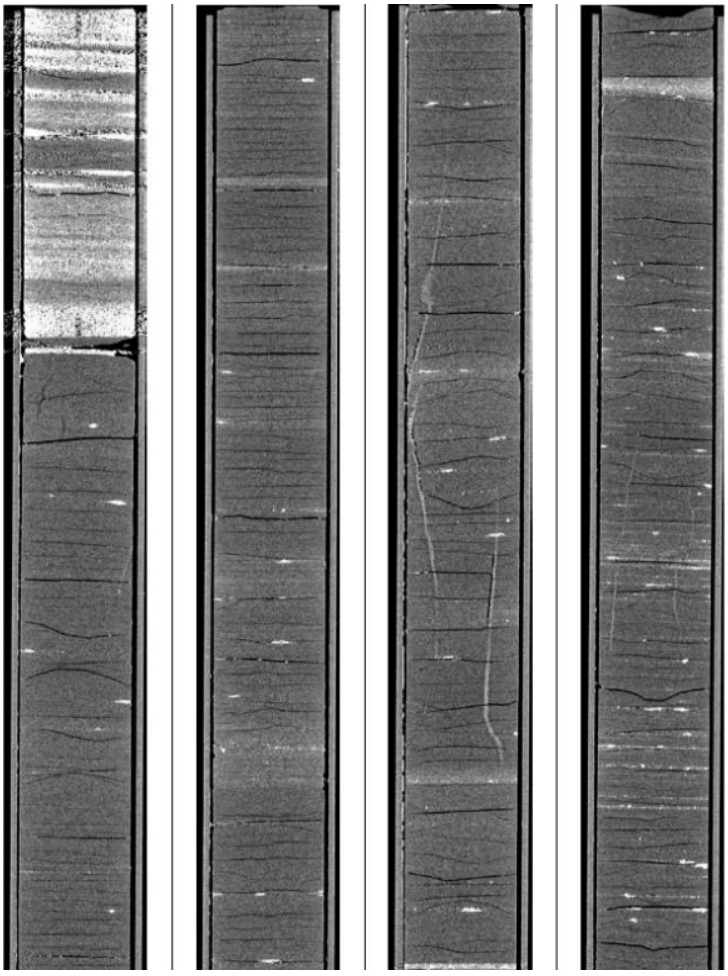

Figure 2 Calcite-filled fractures viewed through CT scan.

The corresponding pole locations were placed into stereonets associated with each stage. This is viewed in **Figure 3** and allows for a better view of the orientation of fractures.

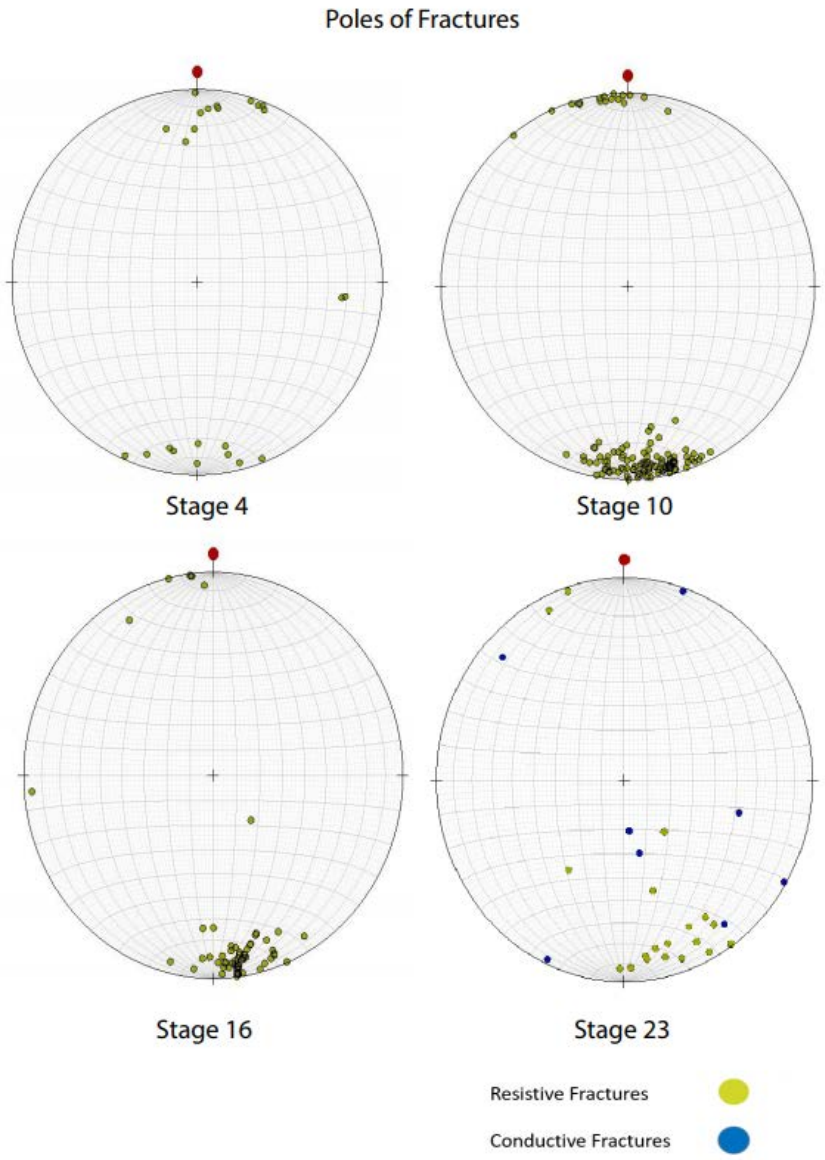

Figure 3 Generated stereonets displaying pole locations of corresponding fracture azimuth values.

Over 1600 natural fractures were identified along the length of the MIP-3H well using image logs (Wilson et al., 2018). Of these pre-existing fractures, 1078 were included within stage locations. Fractures were described as either conductive or resistive (mineral-filled). The resistive fractures (n = 1068) are more abundant than the conductive fractures (n = 10). Most of the conductive fractures were clustered in stage 23 (Figure 2) with an average trend of N72°E. Fractures were classified as resistive or conductive based on whether the fractures were mineral-filled or not respectively.

When performing the Mohr circle analysis on these pre-existing fractures, the average treatment pressure of each individual stage was applied. The overall average treatment pressure for the stages

was 8,502 psi. Stage and treatment pressure data were obtained from Northeast Natural Energy's stimulation summary report on the MIP-3H well.

The stress state of the area was based on previous studies in the area. Wilson and Sullivan (2016) used microseismic event trends along with the Mohr-Coulomb failure criteria to estimate the orientation of the maximum horizontal stress in the study area. Shmax of the local area has an orientation of N57°E this was determined using micro-seismic event trends (Wilson and Sullivan, 2016). This estimation was completed by orienting Shmax in the direction where the fewest micro-seismic events fell below the failure envelope (Wilson and Sullivan, 2016).

Stress is defined as a force acting on a specified area. This stress can be described using a second-rank tensor with nine components as

Eq.1:

$$S = \begin{bmatrix} S_{11} & S_{12} & S_{13} \\ S_{21} & S_{22} & S_{23} \\ S_{31} & S_{32} & S_{33} \end{bmatrix}$$

where the subscripts of the individual stress components refer to the direction of the force acting on a given face of the infinitesimal cube. Since the cube is not rotating, torque is zero. Therefore, the order of the subscripts will be unimportant as $S_{12} = S_{21}$, $S_{13} = S_{31}$ and $S_{23} = S_{32}$.
The principal normal stress is represented by

Eq. 2:

$$S = \begin{bmatrix} S_1 & 0 & 0 \\ 0 & S_2 & 0 \\ 0 & 0 & S_3 \end{bmatrix}$$

This stress can be expressed in a geographical coordinate system using the transform

Eq. 3:

$$S_g = R_1' S R_1$$

where

Eq. 4:

$$R_1 = \begin{bmatrix} \cos\alpha\cos\beta & \sin\alpha\cos\beta & -\sin\beta \\ \cos\alpha\sin\beta\sin\gamma - \sin\alpha\cos\gamma & \sin\alpha\sin\beta\sin\gamma + \cos\alpha\cos\gamma & \cos\beta\sin\gamma \\ \cos\alpha\sin\beta\cos\gamma + \sin\alpha\sin\gamma & \sin\alpha\sin\beta\cos\gamma - \cos\alpha\sin\gamma & \cos\beta\cos\gamma \end{bmatrix}$$

$\alpha, \beta, and\ \gamma$ are the rotation angles that define the stress coordinate system in terms of geographic coordinates.

The geographic coordinate system created using stress tensors and fracture orientation discussed above were used in the application of Cauchy's Stress Theorem. This coordinate system (North-East-Down) was used when applying the theorem to every fracture at each stage to calculate normal and shear stress components. Cauchy's Stress Theorem is shown in the Eq.5 where $\vec{T}$ represents the vector value of the traction on a plane with respect to the normal vector $\vec{n}$, and $\vec{\sigma}^T$ denotes the transposed stress tensor.

Eq. 5:

$$\vec{T} = \vec{\sigma}^T \cdot \vec{n}$$

This traction vector $\vec{T}$ is the value limiting the ratio of force over a surface, while *n* indicates the normal to that surface. The normal vector can be used to determine the traction vector that is acting on the plane. In this case, the planes being analyzed are the pre-existing fractures within the MIP-3H well. The transposed matrix (σ^T), Cauchy's Stress Tensor, in the formula above represents the stress acting on the surface of the fracture. This matrix is written below where "e" represents the unit vectors on the coordinate system.

Eq. 6:

$$\sigma = \begin{bmatrix} \mathrm{Tx}_1{}^{(e1)} & \mathrm{Tx}_2{}^{(e1)} & \mathrm{Tx}_3{}^{(e1)} \\ \mathrm{Tx}_1{}^{(e2)} & \mathrm{Tx}_2{}^{(e2)} & \mathrm{Tx}_3{}^{(e2)} \\ \mathrm{Tx}_1{}^{(e3)} & \mathrm{Tx}_2{}^{(e3)} & \mathrm{Tx}_3{}^{(e3)} \end{bmatrix}$$

Failure of pre-existing fractures was identified by applying the stresses on each fracture in a Mohr diagram. A Mohr diagram was created for each individual stage and the accompanying fractures. For a fracture to undergo tensile failure, the strength or resistance of the fracture must be overcome (Zoback, 2010). Once the fracture starts to grow in length and exceeds several tens of cm, only a small amount of pressure above the minimum horizontal stress is required to extend those fractures (Zoback, 2010).

Results

Existing research on fracture activation in the subsurface combined with fracture failure data discussed here shows that all fractures, healed and open, are activated during hydraulic fracturing. Using data obtained from the MSEEL project, fracture location was plotted onto a three-dimensional Mohr diagram for each of the stages in the MIP-3H well. The stress tensors from each stage along with the strike and dip of each pre-existing fracture was used to plot the data points.

Figure 4 shows the graphical representation of the fracture in the four stages viewed in this paper. The diagrams show the stress states before and during the frac. The right circle shows the stress state before the frac with natural pore pressure applied. The circle on the left side of the graph

shows the stress state with treatment pressure applied. During hydraulic fracturing the fractures enter the tensile failure regime. Research by Kavousi et al. 2017, showed that fractures within the core of the MIP-3H failed during tensile testing.

Three principal stresses (Sv, Shmax, and Shmin) were determined based on geologic information from the Marcellus Shale formation surrounding the study area. Based on the results of this research, it is concluded that all pre-existing fractures, mineral-filled and open, were activated during the fracture process.

Discussion

Research conducted on the tensile failure of fractures within the MIP-3H core lead to similar results as discussed above. These pre-existing fractures failed even when calcite-filled. The analysis conducted showed a connection between the P32 fracture intensity and the distribution of fiber optic hDVS energy. Stages with more pre-existing fractures vibrated less than those with a low P32. This showed the connection between fracture intensity and hydraulic fracturing efficiency. The lower the P32, the more energy was required to induce fractures. A higher P32 resulted in less hDVS required, because the rock was more easily broken. Because all pre-existing fractures experienced tensile failure during hydraulic fracturing, the calcite fill has very little to no effect on hydraulic fracturing efficiency (Kavousi, et al., 2017).

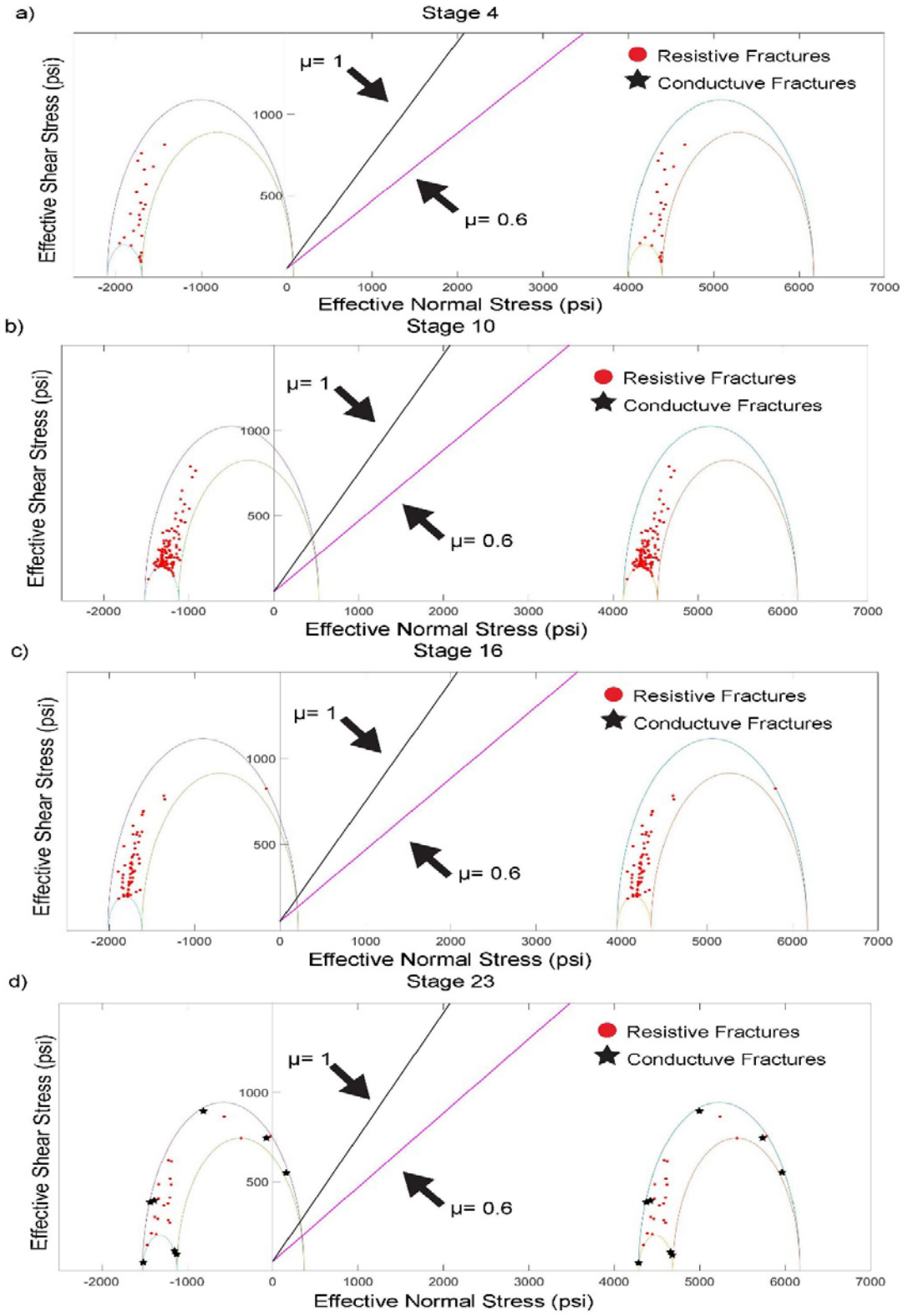

Figure 3 Fractures in four stages of the MIP-3H well plotted on a Mohr diagram. Conductive fractures in all stages show the same trends in the Mohr Circle. Conductive fractures shown as stars are located along the edge of the circle.

Conclusions

Wireline image logs were used to identify natural fractures within the lateral portion of the well. The contrast between calcite, which fills most fractures within the Marcellus, and shale allowed for easy identification of these fractures. Over 1600 of the pre-existing fractures present were resistive, calcite-filled, as well as a few conductive, or open, fractures. The behavior of pre-existing fractures when exposed to high pressures during hydraulic stimulation may lead to a better understanding of variables impacting stimulation efficiency and overall recovery efficiency of unconventional, shale-gas wells.

Natural fractures make up much of the permeability that allows for gas flow in unconventional shale wells, so it is key that these fractures open during stimulation of the reservoir. Data sourced from a Marcellus Shale well in northern West Virginia, U.S.A allowed for failure analysis of naturally-occurring fractures under regional geologic stresses as pressure is introduced during stimulation. Over 1600 fractures were plotted on Mohr diagrams representing pressures before and during hydraulic stimulation for each stage using the stress values of the area and treatment pressures. The analysis showed that all fractures, whether resistive or conductive, underwent tensile failure. This shows that all fractures are contributing to the permeability of the reservoir after the hydraulic fracturing process.

Acknwledgements

This research is funded through the U.S.DOE National Energy Technology Lab part of their Marcellus Shale Energy and Environmental Laboratory (MSEEL) (DOE Award No.: DE-FE0024297). Matlab software was used for much of the analysis. A special thanks to Northeast Natural Energy, Schlumberger, WVU and all other companies and organizations involved with the MSEEL project.

References

Bhattacharya, S., Kavousi, P., Carr, T., Pantaleone, S., 2019, Application of predictive data analytics to model daily hydrocarbon production using petrophysical, geochemical, fiber-optic, completions, and surface data: A case study from the Marcellus Shale, North America: Journal of Petroleum Science and Engineering, **176**, 702-715

Chen, Ruiqian, and Shikha Sharma. "Linking the Acadian Orogeny with organic-rich black shale deposition: Evidence from the Marcellus Shale." *Marine and Petroleum Geology* 79 (2017): 149-158.

Engelder, T., Lash, G.G., 2009, Joint sets that enhance production from Middle and Upper Devonian gas shales of the Appalachian Basin: AAPG Bulletin, **93,** 857-889, doi:10.1306/03230908032

Lash G. G., Engelder T. 2011. Thickness trends and sequence stratigraphy of the MiddleDevonian Marcellus Formation, Appalachian Basin: Implications for Acadian foreland basin evolution. *AAPG bulletin*, *95*(1), 61-103.

Kavousi, Payam, Timothy Carr, Thomas Wilson, Shohreh Amini, Collin Wilson, Mandy Thomas, Keith MacPhail et al. "Correlating distributed acoustic sensing (DAS) to natural fracture intensity for the Marcellus Shale." In *SEG Technical Program Expanded Abstracts 2017*, pp. 5386-5390. Society of Exploration Geophysicists, 2017

Wang G., Carr T.R., 2013. Organic-rich Marcellus Shale lithofacies modeling and distribution pattern analysis in the Appalachian basin. *AAPG bulletin, 97*(12), 2173-2205

Wang G., Carr T.R., 2012. Methodology of organic-rich shale lithofacies identification and prediction: A case study from Marcellus Shale in the Appalachian Basin.*Computers and Geoscience, 49,* 151-163

Wilson T.H., Carr T.R., Carney B J., Yates M., MacPhail K., Morales A., Costello I., Hewitt J., Jorden E., Uschner N., Thomas M., Akin S., Magbagbeola O., Johansen A., Hogarth L., Anitowoshe O., Naseem K., 2018, Marcellus Shale model stimulation tests and microseismic response yield insights into mechanical properties and the reservoir discrete fracture network: *Interpretation, 6*(2), 1-50, doi:10.1190/INT-2016-0199.1

Wilson T.H., Sullivan P., 2016, Microseismic energy density and event trend constraints on model DFN development for hydraulically fractured reservoirs: Marcellus shale, south western Pennsylvania, U.S.A.: 86th Annual International Meeting, SEG, Expanded Abstracts, 3093-3097, doi: 10.1190/segam2016-13528380.1.

Zoback, M. D., 2010, Reservoir geomechanics: CambridgeUniversity Press.

U.S EIA, 2019. Natural Gas. *Annual Energy Outlook 2019 with Projections to 2050*. 69-86

Timothy R Carr, Thomas H. Wilson, Payam Kavousi, Shohreh Amini, Shikha Sharma, West Virginia University: Jay Hewitt, Ian Costello, B. J. Carney, Emily Jordon, Northeast Natural Energy LLC: Malcolm Yates, Keith MacPhail, Natalie Uschner, Mandy Thomas, Si Akin, Oluwaseun Magbagbeola, Adrian Morales, Asbjoern Johansen, Leah Hogarth, Olatunbosun Anifowoshe, Kashif Naseem, Schlumberger: Richard Hammack, Abhash Kumar, Erich Zorn, Robert Vagnetti, and Dustin Crandall, National Energy Technology Laboratory, US Department of Energy., 2017, Insights from the Marcellus Shale Energy and Environment Laboratory (MSEEL), Unconventional Resources Technology Conference, Austin, July 2017 , DOI 10.15530-urtec-2017-2670437

National Energy Technology Laboratory

626 Cochrans Mill Road
P.O. Box 10940
Pittsburgh, PA 15236-0940

3610 Collins Ferry Road
P.O. Box 880
Morgantown, WV 26507-0880

13131 Dairy Ashford Road, Suite 225
Sugar Land, TX 77478

1450 Queen Avenue SW
Albany, OR 97321-2198

Arctic Energy Office
420 L Street, Suite 305
Anchorage, AK 99501

Visit the NETL website at:
www.netl.doe.gov

Customer Service Line:
1-800-553-7681